

# An Investigation of Gravity-Driven Particle-Laden Flow Down an Incline and Hindered Settling

Scott Bloom<sup>1</sup>, Albert Baeumer<sup>1</sup>, Davis Funk<sup>2</sup>, Cameron Hatler<sup>3</sup>, Qitong Luan<sup>1</sup>, Malia K. Mitchell<sup>4</sup>, and Moniriddh Bunyay<sup>5</sup>

<sup>1</sup>University of California, Los Angeles, CA 90095, USA

<sup>2</sup>West Virginia University, Morgantown, WV 26506, USA

<sup>3</sup>Pomona College, Claremont, CA 91711, USA

<sup>4</sup>Howard University, Washington, DC 20059, USA

<sup>5</sup>University of California, San Diego, La Jolla, CA 92093, USA

15:00 August 9, 2024

## Abstract

We present theoretical and experimental results of viscous, gravity-driven particle-laden flow down an incline, as well as give a review of current hindrance settling functions, and present our own empirical model for our specific particles. For the particle-laden flow, we look at the ridged regime to analyze mass-shedding, in which a maximum packing fraction particle front gains enough mass to separate from the bulk fluid flow and fall down the incline as a quasi-solid. The settled regime is used to study the bidisperse case, where two distinct particle sizes are present and settle out on different fronts. The objective is to gain insights into the behaviors and interactions of particles in various fluid dynamic scenarios, contributing to the understanding of particle-fluid interactions and improving the accuracy of predictive models.

# Contents

<b>1</b>	<b>Introduction</b>	<b>3</b>
<b>2</b>	<b>Background</b>	<b>4</b>
2.1	Thin Viscous Liquid Film Flowing Down an Incline . . . . .	4
2.2	Monodisperse Particle Laden Flow . . . . .	5
2.3	Bidisperse Particle Laden Flow . . . . .	9
<b>3</b>	<b>Experimental Procedure</b>	<b>10</b>
3.1	Experimental Setup and Materials . . . . .	11
3.2	Particle Dyeing and Sieving . . . . .	12
3.3	Mass Shedding . . . . .	13
3.4	Bidisperse . . . . .	14
3.5	Numerical Simulations . . . . .	14
<b>4</b>	<b>Image Analysis</b>	<b>15</b>
4.1	Finding the Front Profile . . . . .	15
4.2	Laser Height Profile . . . . .	20
<b>5</b>	<b>Results</b>	<b>23</b>
5.1	Bidisperse . . . . .	23
5.1.1	Front Profile . . . . .	23
5.1.2	Spiral Separator . . . . .	24
5.2	Mass-Shedding . . . . .	26
<b>6</b>	<b>Hindered-Settling</b>	<b>29</b>
6.1	Background . . . . .	30
6.1.1	Single Particle . . . . .	31
6.1.2	Monodisperse Settling . . . . .	32
6.1.3	Bidisperse Settling . . . . .	32
6.2	Experimental Procedure . . . . .	33
6.2.1	Single Particle . . . . .	33
6.2.2	Bidisperse Hindered Settling . . . . .	34
6.3	Image Analysis/Results . . . . .	35
<b>7</b>	<b>New &amp; Future Research</b>	<b>39</b>
7.1	Improvements of Experimental Procedures . . . . .	39
7.2	Future Mass Shedding Experiments . . . . .	40
7.3	Mass Shedding Models . . . . .	41
<b>8</b>	<b>Conclusion</b>	<b>42</b>
<b>References</b>		<b>43</b>

# 1 Introduction

Particle-laden flow is defined as a two phase flow involving solid particles suspended in a fluid medium. We investigate these mixtures in thin, viscous films flowing down an incline. They are relevant in many industrial applications, such as in cement mixing and mining, as well as in modeling landslides [8], mineral processing [6], and molten chocolate [9].

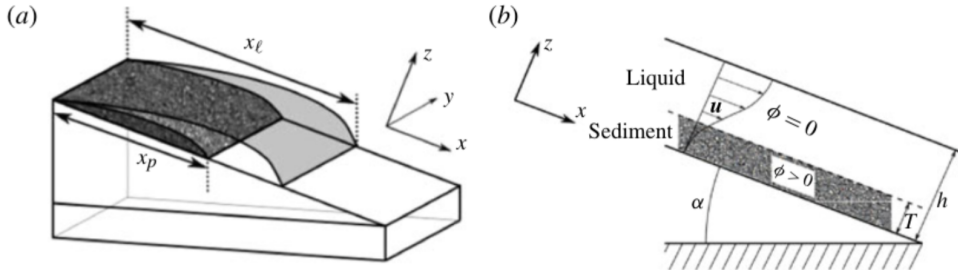


Figure 1: Particle Laden Flow

To characterize the flow, we define variables relevant to the experiment. As seen in 1,  $\phi$  is known as the particle volume fraction, a ratio of the particle's volume to the entire mixture's volume. The track is set at an inclination angle,  $\alpha$ , with respect to the ground, and the length of the track is characterized by its length  $L$  and with a fluid height of  $H$ . The positive  $x$ -direction is denoted as down the incline, while the  $z$ -direction points perpendicular to the ramp.

There are three main regimes that the particles can be found in while traversing the incline: the settled regime, ridged regime, and well mixed regime. The well mixed regime is where the particles are all evenly suspended in the fluid medium. This state is unstable, and if present, will quickly devolve into one of the two other regimes mentioned. The settled regime occurs at low particle volume fractions,  $\phi$ , and at low inclination angles,  $\alpha$ . Here, the particles will settle towards the bottom of the fluid, and the average fluid velocity exceeds that of the average particle velocity, leaving a particle front that lags behind the fluid front. On the other hand, the ridged regime occurs beyond a critical inclination angle and volume fraction, where the particles fall down faster than the fluid. This leads to a ridge at the mixture's front where the particles accumulate, and if heavy enough, can lead to mass shedding where chunks of particles at maximum packing fraction act as a quasi-solid and slide down the incline quickly, just as a solid object would.

Similar to past REU groups, we use the same experimental setup that will be discussed in a later section, and investigate to find the regimes mass shedding occurs, as well as the underlying physics behind the bidisperse case, and how the two particles sizes will move together down the track. Furthermore, we seek to investigate the effects particle-particle interactions can have on the settling of particles in a viscous fluid. As these effects can have a large impact on the bidisperse particle laden flow, we seek to improve the empirically found hindered settling flux through these experiments.

In Section 2 we go over the theory behind the thin film equation, monodisperse particle laden flow and bidisperse particle laden flow. In Section 3 we discuss the experimental procedure around the setup of our inclined slope. We discuss how we dyed our particles and sieved them. We discuss our mass shedding experimental setup and our bidisperse experimental setup. We also provide our numerical simulations. In Section 4 we discuss our image analysis procedure for finding the front profiles and the laser height profile. In Section 5 we discuss the results we gathered in our bidisperse and mass-shedding experiments. In Section 6 we

discuss our approach to trying to improve the hindered-settling function for the bidisperse experiment. This involved discussing the background of hindered-settling and the experimental procedure for this experiment. In Section 7 we discuss possible improvements to our experimental procedures and new experiments for our mass-shedding investigation. We also have a brief discussion of possible model ideas for mass shedding. In Section 8 we conclude with what we achieved during the CAM REU.

## 2 Background

### 2.1 Thin Viscous Liquid Film Flowing Down an Incline

We begin by starting with the continuity and Navier-Stokes equations

$$\begin{aligned} \nabla \cdot \mathbf{u} &= 0, \\ \rho \left( \frac{\partial \mathbf{u}}{\partial t} + (\mathbf{u} \cdot \nabla) \mathbf{u} \right) &= -\nabla p + \mu \nabla^2 \mathbf{u} + \mathbf{g}, \end{aligned} \quad (1)$$

where  $\mathbf{u}$  is the velocity field,  $p$  is the pressure field,  $\rho$  is the fluid density,  $\mu$  is the dynamic viscosity, and  $\mathbf{g}$  is the gravitational force. These equations are for the case where we are just considering a single thin viscous fluid flowing down an incline without any particles within it.

These equations can then be expanded into the  $x$ ,  $y$ , and  $z$  directions as followed given  $\mathbf{g} = g(\sin \alpha \hat{\mathbf{i}} - \cos \alpha \hat{\mathbf{k}})$  so that

$$\frac{\partial u}{\partial x} + \frac{\partial v}{\partial y} + \frac{\partial w}{\partial z} = 0, \quad (2)$$

and component wise for the Navier Stokes equations we find

$$x: \quad \rho \left( \frac{\partial u}{\partial t} + u \frac{\partial u}{\partial x} + v \frac{\partial u}{\partial y} + w \frac{\partial u}{\partial z} \right) = -\frac{\partial p}{\partial x} + \mu \left( \frac{\partial^2 u}{\partial x^2} + \frac{\partial^2 u}{\partial y^2} + \frac{\partial^2 u}{\partial z^2} \right) + \rho g \sin \alpha, \quad (3)$$

$$y: \quad \rho \left( \frac{\partial v}{\partial t} + u \frac{\partial v}{\partial x} + v \frac{\partial v}{\partial y} + w \frac{\partial v}{\partial z} \right) = -\frac{\partial p}{\partial y} + \mu \left( \frac{\partial^2 v}{\partial x^2} + \frac{\partial^2 v}{\partial y^2} + \frac{\partial^2 v}{\partial z^2} \right), \quad (4)$$

$$z: \quad \rho \left( \frac{\partial w}{\partial t} + u \frac{\partial w}{\partial x} + v \frac{\partial w}{\partial y} + w \frac{\partial w}{\partial z} \right) = -\frac{\partial p}{\partial z} + \mu \left( \frac{\partial^2 w}{\partial x^2} + \frac{\partial^2 w}{\partial y^2} + \frac{\partial^2 w}{\partial z^2} \right) - \rho g \cos \alpha. \quad (5)$$

These equations can then be scaled using specific characteristic scales relevant to our experiment to non-dimensionalise the Navier-Stokes equation and simplify them down based on assuming certain terms are much less than the dominating terms in the equation. The process is as follows with scaling parameters:

$$\begin{aligned} \bar{x} &= \frac{x}{L}, & \bar{y} &= \frac{v}{L}, & \bar{z} &= \frac{z}{H}, & \bar{u} &= \frac{u}{U}, & \bar{v} &= \frac{v}{U}, & \bar{w} &= \frac{w}{\epsilon U}, & \bar{p} &= \frac{p}{\rho^* H U^2}, & \bar{t} &= \frac{U}{L} t, & \bar{\mu} &= \frac{\mu}{\mu^*}, & \bar{\rho} &= \frac{\rho}{\rho^*}, \\ \epsilon &= \frac{H}{L}. \end{aligned} \quad (6)$$

Here we introduce a new parameter  $\epsilon$  representing the ratio of the height of the fluid film to the length of the track. With thin films, we can assume  $\epsilon \ll 1$ , which will allow us to reduce by ignoring terms of higher order  $\epsilon$  as being sufficiently small enough to not effect our model. As a small side note, the scaling for  $\bar{w}$  can

be pulled out of the incompressibility condition as a way to conserve conservation of mass.

$$\frac{U}{L}\bar{u}_x + \frac{U}{L}\bar{v}_y + \frac{W}{H}\bar{w}_x = 0, \quad (7)$$

$$\implies \bar{u}_x + \bar{v}_y + \frac{LW}{HU}\bar{w}_x = 0, \quad (8)$$

$$\implies W = \frac{H}{L}U = \epsilon U. \quad (9)$$

Combining equations 8 and 9 we thus get  $\frac{LW}{HU} = O(1)$  and can preserve the conservation of mass.

$$\bar{u}_x + \bar{v}_y + \bar{w}_x = 0. \quad (10)$$

Non-dimensionalising in the  $x$  direction, we get

$$\frac{H}{\mu^*} \left[ \left( \frac{\rho^* U^2}{L} \bar{\rho} \frac{D\bar{u}}{Dt} \right) = -\frac{\rho^* U^2}{\mu^* L} \frac{\partial \bar{p}}{\partial \bar{x}} + \mu^* \mu \left( \frac{U}{L^2} \frac{\partial^2 \bar{u}}{\partial \bar{x}^2} + \frac{U}{L^2} \frac{\partial^2 \bar{u}}{\partial \bar{y}^2} + \frac{U}{H^2} \frac{\partial^2 \bar{u}}{\partial \bar{z}^2} + \frac{p^* L^3}{U^2} \bar{p} \bar{g} \sin \alpha \right) \right], \quad (11)$$

$$\implies \text{Re} \frac{U \bar{\rho} D\bar{u}}{L Dt} = -\frac{U}{L} \frac{\partial \bar{p}}{\partial \bar{x}} + \bar{\mu} \epsilon \frac{U}{L} \left( \frac{\partial^2 \bar{u}}{\partial \bar{x}^2} + \frac{\partial^2 \bar{u}}{\partial \bar{y}^2} \right) + \bar{\mu} \frac{U}{H} \frac{\partial^2 \bar{u}}{\partial \bar{z}^2} + \frac{H p^* L^3}{U^2 \mu^*} \bar{p} \bar{g} \sin \alpha, \quad (12)$$

$$\implies \text{Re} \cancel{\frac{U \bar{\rho} D\bar{u}}{L Dt}} = -\frac{U}{L} \frac{\partial \bar{p}}{\partial \bar{x}} + \bar{\mu} \epsilon \frac{U}{L} \left( \frac{\partial^2 \bar{u}}{\partial \bar{x}^2} + \frac{\partial^2 \bar{u}}{\partial \bar{y}^2} \right) + \bar{\mu} \frac{U}{H} \frac{\partial^2 \bar{u}}{\partial \bar{z}^2} + \frac{H p^* L^3}{U^2 \mu^*} \bar{p} \bar{g} \sin \alpha. \quad (13)$$

Here Reynolds number is defined as the ratio of inertial to viscous forces, and under sufficiently slow fluids we find that

$$\text{Re} := \frac{\rho v L}{\mu} \ll 1. \quad (14)$$

By ignoring the  $y$  component, we can apply the Laplace-Young BC (while ignoring curvature), the no slip boundary condition, and the requirement of stress continuity to solve the equation in the  $x$  and  $z$  components to find an explicit expression for  $\mathbf{v} = (u, v)^T$  such that

$$\mathbf{v} = \left[ \frac{1}{\mu} \nabla_2 P - \frac{\rho g}{\mu} \sin \alpha \hat{\mathbf{i}} \right] \left[ \frac{z^2}{2} - h z \right]. \quad (15)$$

Hence, after averaging this expression with respect to  $z$  we are left needing to solve for  $h$ , given by the **Thin Film Equation**:

$$\partial_t h = \frac{1}{3\mu} \nabla \cdot [\rho g h^3 (\cos \alpha \nabla h - \sin \alpha \hat{\mathbf{i}})], \quad (16)$$

By neglecting the cosine term we are able to solve this using typical conservation law methods and compute **Huppert's Solution** [7]:

$$h = \left( \frac{\nu}{g \sin \alpha} \right)^{1/2} \left( \frac{x}{t} \right)^{1/2}, \quad 0 \leq x \leq x_N = \left( \frac{9A^2 g \sin \alpha t}{4\nu} \right)^{1/3}. \quad (17)$$

## 2.2 Monodisperse Particle Laden Flow

The main goal of this section is to discuss how the Navier-Stokes/Thin Film Equations derived in Section 2.1 is used to describe particle laden flow as in [12]. We consider a suspension consisting of a viscous incompressible fluid and rigid spherical monodisperse non-colloidal particles. We focus on the settled regime, where a layer of dense, sedimentary particles has formed close to the surface of the incline, and a clear layer of fluid flows

on top of it as shown in Figure 1(a). Again the flows are assumed to be symmetrical in the  $y$ -direction, so it suffices to consider just a cross-section of the setup illustrated in Figure 1(b). In particular,  $\mathbf{u} = (u, w)^T$ , and we only consider the  $x$  and  $z$ -directions for all spatial derivatives.

We denote by  $\phi$  the particle volume fraction, a ratio of the particle's volume to the entire mixture's volume. Since we assume that the particles are spheres with the same size, there exists an upper bound (called the max packing fraction)  $\phi_m < 1$  of  $\phi$ . Due to the presence of particles, the viscosity  $\mu$  is now a function of  $\phi$ . Because we no longer have homogeneous density, we now need to express the density as a combination of particle density  $\rho_p$  and liquid density  $\rho_\ell$  [12]:

$$\rho = \rho_p\phi + \rho_\ell(1 - \phi). \quad (18)$$

We will again use the Navier-Stokes equations for our modeling. We first perform some reductions by a re-scaling argument. Let  $L$  be the length scale of  $x$  and  $H$  be the length scale of  $z$ . In addition, let  $U$  be the velocity scale in the  $x$ -direction,  $\rho^*$  be the density scale, and  $\mu^*$  be the viscosity scale. We define the Reynolds number by

$$Re = \frac{\rho^* H U}{\mu^*}. \quad (19)$$

In our scenario, we can assume that the Reynolds number is negligibly small [12], since we are using a viscous oil and therefore observe slow creeping flow. Next we introduce the dimensionless variables

$$\hat{x} = \frac{x}{L}, \quad \hat{z} = \frac{z}{H}, \quad \hat{t} = \frac{tU}{L}, \quad \hat{u} = \frac{u}{U}, \quad \hat{w} = \frac{w}{U}, \quad \hat{p}^D = \frac{p^D}{\rho U^2}, \quad (20)$$

where the superscript  $D$  signifies the dynamic pressure incorporating the effect of gravity. Substituting the scales defined in (20) into Equation (1), we have

$$\frac{D\hat{\mathbf{u}}}{Dt} = -\hat{\nabla}\hat{p}^D + \frac{1}{Re}\hat{\nabla}^2\hat{\mathbf{u}}. \quad (21)$$

Since  $Re$  is small,  $1/Re$  is large, so the term  $1/Re\hat{\nabla}^2\hat{\mathbf{u}}$  is significant. We should further remark that the pressure gradient in the dimensionless form is purposefully made independent of the Reynolds number to avoid singularities in the pressure gradient as the Reynolds number tends to zero. It is nonetheless a significant term in the equation. On the other hand, the left-hand side of Equation (21) makes a negligible contribution [14]. Reverting back to the dimensional variables, we now have

$$\mathbf{0} = -\nabla p + \nabla \cdot (\mu(\nabla \mathbf{u} + \nabla \mathbf{u}^T)) + \rho \mathbf{g}. \quad (22)$$

Substituting the density expression in (18) into Equation (22), we now have

$$\nabla p - \nabla \cdot (\mu(\phi)(\nabla \mathbf{u} + \nabla \mathbf{u}^T)) = (\rho_p\phi + \rho_\ell(1 - \phi))\mathbf{g} \quad (23)$$

for  $0 \leq \phi \leq \phi_m$ .

By a similar process to how we derived the Navier-Stokes equations, we can derive the following equation for conservation of particle volume

$$\frac{\partial \phi}{\partial t} + \mathbf{u} \cdot \nabla \phi + \nabla \cdot \mathbf{J} = 0, \quad (24)$$

where  $\mathbf{J} = (J_x, J_z)^T$  represents the particle flux.

We now specify the following boundary conditions for equations (23) and (24):

1. The non-slip and impermeability condition at the solid substrate:  $u = w = 0$  at  $z = 0$ ;
2. The zero-stress condition at the free surface:  $(-p\mathbb{I} + \mu(\phi)(\nabla \mathbf{u} + \nabla \mathbf{u}^T))\mathbf{n} = 0$  at  $z = h$ ;
3. The zero-particle-flux condition at both surfaces:  $\mathbf{J} \cdot \mathbf{n} = 0$  at  $z = 0$  and  $z = h$ ;
4. The kinematics condition for free surface evolution:  $\partial_t h = w - u\partial_x h$  at  $z = h$  at  $z = h$ .

Here,  $\mathbf{n}$  is the outward pointing normal at the two surfaces.

Equations (23) and (24), together with all of the boundary conditions are very difficult to solve, so we will use lubrication approximations to further simplify them in this section. Let  $\mu_\ell$  be the viscosity of the fluid and  $d$  be the diameter of the particles. We define the following scales

$$\begin{aligned} x &= \frac{H}{\epsilon}\tilde{x}, z = H\tilde{z}, \phi = \tilde{\phi}, \mu = \mu_\ell\tilde{\mu}, u = U\tilde{u} = \frac{H^2\rho eg \sin \alpha}{\mu_\ell}\tilde{u}, \\ w &= \epsilon U\tilde{w}, t = \frac{H}{\epsilon U}\tilde{t}, J_z = \frac{d^2U}{H^2}\tilde{J}_z, J_x = \frac{\epsilon d^2U}{H^2}\tilde{J}_x, p = \frac{U\mu_\ell}{H}\tilde{p}, \end{aligned} \quad (25)$$

where  $\epsilon$  is a small lubrication-style parameter related to the equilibrium requirement we will discuss next.

We want to derive a continuum model in which the particle flux in the  $z$ -direction is in equilibrium, and according to [12], this can be achieved by requiring

$$\epsilon \ll \left(\frac{d}{H}\right)^2 \ll 1, \quad (26)$$

and mathematically, a way to satisfy (26) is to set  $(d/H)^2 = \epsilon^\beta$  for some  $0 < \beta < 1$ . Now applying the scales in (25) and the definition of  $\beta$  to Equation (24), we have that

$$\partial_t \phi + u\partial_x \phi + w\partial_z \phi = -\epsilon^{\beta+1}\partial_x J_x - \epsilon^{\beta-1}\partial_z J_z, \quad (27)$$

where we drop all tildes for simplicity. We now define the asymptotic expansions of the solution:

$$\begin{aligned} \phi(t, x, z) &= \phi^0(t, x, z) + o(1), u(t, x, z) = u^0(t, x, z) + o(1), \\ w(t, x, z) &= w^0(t, x, z) + o(1), h(t, x) = h^0(t, x) + o(1), \\ J_x(t, x, z) &= J_x^0(t, x, z) + o(1), J_z(t, x, z) = J_z^0(t, x, z) + o(1), \\ &\text{where } \phi^0, u^0, w^0, h^0, J_x^0, J_z^0 \sim O(1). \end{aligned} \quad (28)$$

Apply these expansions in Equation (27), and we have that the leading order term is  $O(\epsilon^{\beta-1})$ . Integrating this term with respect to  $z$  and employing the zero-particle-flux boundary conditions yields

$$J_z^0(t, x, z) = J_z^0|_{z=0} = J_z^0|_{z=h} = 0. \quad (29)$$

By a similar approach on the  $x$ -component of Equation (23), we have that

$$\partial_z(\mu(\phi^0)\partial_z u^0) = -1 - \frac{\rho_p - \rho_\ell}{\rho_\ell \phi^0}, \quad (30)$$

coupled with the non-slip and zero-stress boundary conditions  $u^0(z = 0) = 0$  and  $\mu(\phi^0)\partial_z u^0 = 0$  [12].

We can then define an integrated volume fraction,  $n(t, x)$ , which we will use to later define our system of conservation laws

$$n(t, x) = \int_0^{h^0} \phi^0(t, x, z) dz. \quad (31)$$

By considering the higher order terms of Equation (27), and including a correction for z direction particle flux, we arrive at the following expression

$$\partial_t \phi^0 + u^0 \partial_x \phi^0 + w^0 \partial_z \phi^0 = \epsilon^{\beta-1} \partial_z (J_z - J_z^0). \quad (32)$$

We then integrate each side of this equation with respect to z from  $z = 0$  to  $z = h^0$  and apply the kinematic condition to find

$$\partial_t \int_0^{h^0} \phi^0 dz = \phi^0(w^0 - u^0 \partial_x h^0)|_{z=h^0} - \int_0^{h^0} u^0 \partial_x \phi^0 dz - \int_0^{h^0} w^0 \partial_z \phi^0 dz. \quad (33)$$

Through extensive manipulation, including the use of integration by parts, the chain rule, along with the incompressibility and impermeability conditions, we arrive at the following equation

$$\partial_t \int_0^{h^0} \phi^0 dz + \partial_x \int_0^{h^0} \phi^0 u^0 dz = 0. \quad (34)$$

By noticing the left integral is the definition of the integrated volume fraction, n, we can then arrive at our first conservation law. Through a similar argument involving the conservation of mass, we can define our second conservation law - giving us the following system

$$\partial_t n + \partial_x \int_0^{h^0} \phi^0(t, x; z) u^0(t, x; z) dz = 0, \quad (35a)$$

$$\partial_t h^0 + \partial_x \int_0^{h^0} u^0(t, x; z) dz = 0, \quad (35b)$$

as seen in [11]. Paired with the boundary conditions  $u^0 = 0$  at  $z = 0$ ,  $\mathbf{J}_z^0|_{z=0} = 0$ , and  $\mu(\phi^0) \partial_z u^0 = 0$  at  $z = h^0$  provides us with a full theoretical framework to be able to solve the problem. We now use the flux function used in [11], where we consider a general particle flux expression based on the diffusive flux theory

$$\mathbf{J} = -\frac{d^2}{4} \left[ K_c \phi \begin{pmatrix} \partial_x (\dot{\gamma} \phi) \\ \partial_z (\dot{\gamma} \phi) \end{pmatrix} + \frac{K_v \phi^2 \dot{\gamma}}{\mu(\phi)} \frac{d\mu(\phi)}{d\phi} \begin{pmatrix} \partial_x \phi \\ \partial_z \phi \end{pmatrix} \right] + \frac{d^2 (\rho_p - \rho_l) \Phi(\phi)}{18\mu(\phi)} \phi \mathbf{g}. \quad (36)$$

In this equation,  $d$  is the particle diameter,  $K_v$  and  $K_c$  are empirically determined constants,  $\dot{\gamma}$  is the strain rate,  $\mu(\phi)$  is the effective viscosity term, and  $\Phi(\phi)$  is the hindered settling function which will be discussed in greater detail later in the paper.

By following the same asymptotic expansion and scaling introduced earlier, we arrive at this simplified version of the flux

$$\mathbf{J}_z^0 = -\frac{K_c}{4} \phi^0 \partial_z (\phi^0 \partial_z u^0) - \frac{K_v}{4} \frac{(\phi^0)^2 \partial_z u^0 \partial_z \phi^0}{\mu(\phi^0)} \frac{d\mu(\phi^0)}{d\phi^0} - \frac{(\rho_p - \rho_l) \Phi(\phi^0) \phi^0 \cot \alpha}{18\rho_l \mu(\phi^0)} \quad (37)$$

Given the relationship of stress in laminar flow,  $\sigma^0 = \mu(\phi^0) \partial_z u^0$ , we can rewrite Equations (23) and (24), giving us a set of ODE's,

$$\phi^0 \partial_z \sigma^0 + \left( 1 + \frac{\phi^0}{\mu(\phi^0)} \frac{d\mu(\phi^0)}{d\phi^0} \frac{K_v - K_c}{K_c} \right) \sigma^0 \partial_z \phi^0 + \frac{2(\rho_p - \rho_l) \Phi(\phi^0) \cot \alpha}{9\rho_l K_c} = 0, \quad (38a)$$

$$\partial_z \sigma^0 = - \left( 1 + \frac{\rho_p - \rho_l}{\rho_l} \phi^0 \right), \quad (38b)$$

which can be solved in combination with our conservation laws. We can rewrite the two previously defined conservation laws in the form

$$\partial_t h + \partial_x F(h, n) = 0, \quad (39a)$$

$$\partial_t n + \partial_x G(h, n) = 0. \quad (39b)$$

By applying the change of variables  $s = z/h^0$ , where  $h^0$  is the leading order term for the film height, we can find the following expressions for the fluxes F and G where

$$F(h, n) = \int_0^h u(t, x; z) dz = h^3 \int_0^1 \tilde{u}(t, x; s) ds = h^3 f(\phi_0), \quad (39c)$$

$$G(h, n) = \int_0^h \phi(t, x; z) u(t, x; z) dz = h^3 \int_0^1 \tilde{\phi}(t, x; s) \tilde{u}(t, x; s) ds = h^3 g(\phi_0). \quad (39d)$$

Here,  $\phi_0$  is the vertically averaged volume fraction, given as

$$\phi_0(t, x) = \int_0^1 \tilde{\phi}(t, x; s) ds = \frac{n(t, x)}{h(t, x)} \in [0, \phi_m], \quad (39e)$$

By choosing a hindered settling function of  $\Phi(\tilde{\phi}) = (1 - \tilde{\phi})$ , and collecting terms into the constant, B, we come up with a simplified version of our previously defined ODE system

$$\left( 1 + \frac{\tilde{\phi}}{\mu(\tilde{\phi})} \frac{d\mu(\tilde{\phi})}{d\tilde{\phi}} \frac{K_v - K_c}{K_c} \right) \tilde{\sigma} \tilde{\phi}' + B - (B + 1)\tilde{\phi} - \frac{\rho_p - \rho_l}{\rho_l} \tilde{\phi}^2 = 0, \quad (39f)$$

$$\tilde{\sigma}' = - \left( 1 + \frac{\rho_p - \rho_l}{\rho_l} \tilde{\phi} \right). \quad (39g)$$

Setting  $\tilde{\phi}' = 0$  in Equation (39f), a critical particle volume fraction can be determined that determines the theoretical transition from the settled to ridged regime, as given by

$$\tilde{\phi}_{crit} = \min \left\{ \phi_m, \frac{-\rho_l (B + 1)}{2(\rho_p - \rho_l)} + \sqrt{\left( \frac{\rho_l (B + 1)}{2(\rho_p - \rho_l)} \right)^2 + \frac{\rho_l B}{\rho_p - \rho_l}} \right\}. \quad (40)$$

### 2.3 Bidisperse Particle Laden Flow

In this section, we extend the modeling in Section 2.2 to bidisperse particle laden flow, i.e., two species of particles of the same density but different sizes. We will still use Equation (23) for momentum balance but will have an equation for the conservation of particle volume for each species

$$\frac{\partial \phi_i}{\partial t} + \mathbf{u} \cdot \nabla \phi_i + \nabla \cdot (\mathbf{J}_i) = 0, \quad i = 1, 2, \quad (41)$$

where the particle flux for each species is given by

$$\mathbf{J}_i = \mathbf{J}_{\text{settling},i} + \mathbf{J}_{\text{shear}} + \mathbf{J}_{\text{tracer},i}, \quad i = 1, 2. \quad (42)$$

The tracer flux, given by

$$\mathbf{J}_{\text{tracer},i} = -\frac{\dot{\gamma}d_i^2}{4}D_{tr}(\phi) \phi \nabla \left( \frac{\phi_i}{\phi} \right),$$

is added to describe the mixing between particle species due to shear-induced migration [16].

Using approximations similar to the ones applied to the monodisperse case, we arrive at the following system of conservation laws

$$\partial_t h + \partial_x \left( h^3 \int_0^1 u ds \right) = \partial_t h + \partial_x (h^3 f(\phi_{0,1}, \phi_{0,2})) = 0 \quad (43a)$$

$$\partial_t n_i + \partial_x \left( h^3 \int_0^1 \phi_i u ds \right) = \partial_t n_i + \partial_x (h^3 g(\phi_{0,1}, \phi_{0,2})) = 0, \quad i = 1, 2. \quad (43b)$$

The derivations of the equilibrium equations are also very similar to the ones in the monodisperse case but with the tracer term. We arrive at the following ODEs

$$\sigma' + \left( 1 + \frac{\rho_p - \rho_\ell}{\rho_\ell} \phi \right) = 0 \quad (44a)$$

$$\chi' = \frac{2 \cot \alpha}{9} \rho_s \frac{(1-\phi)(1-\chi)(\chi)((2\chi-1)d_1^2 d_2^2 + a(d_1^2 - (d_1^2 + d_2^2)\chi))}{\sigma(\bar{a}K_c \phi \chi(1-\chi) + D_{tr}(\phi)(d_1^2 d_2^2(1-\chi)^2 + a(d_1^2 + d_2^2)(1-\chi)(\chi) + d_1^2 d_2^2 \chi^2))} \quad (44b)$$

$$\begin{aligned} \phi' = & -\frac{((\chi + ad_2^{-2}(1-\chi)h_1) + ((1-\chi) + ad_1^{-2}\chi)h_2)\chi' + (2\cot \alpha/9)\rho_s(1-\phi)}{g(\chi^2 + a(d_1^{-2} + d_2^{-2})\chi(1-\chi) + (1-\chi^2))} \\ & - \frac{K_c \phi \sigma' (\chi^2 + a\chi(1-\chi)(d_1^{-2} + d_2^{-2}) + (1-\chi)^2)}{g(\chi^2 + a(d_1^{-2} + d_2^{-2})\chi(1-\chi) + (1-\chi^2))}, \end{aligned} \quad (44c)$$

with the boundary condition

$$\sigma(1) = 0 \quad (45)$$

and the integration condition

$$\int_0^1 \phi_i(t, x, s) ds = \phi_{0,i}, \quad i = 1, 2, \quad (46)$$

where

$$a = \frac{1}{4} \frac{(d_1 + d_2)^4}{8(d_1^2 + d_2^2)}$$

and

$$\bar{a} = \frac{1}{4} \left( d_1^2 d_2^2 - \frac{(d_1 + d_2)^{10}}{64(d_1^3 + d_2^3)^2} \right)^{\frac{1}{2}}.$$

### 3 Experimental Procedure

A variety of experiments were performed during the program - two of which used the same basic experimental set up.

---

<sup>1</sup>The calculations for the bidisperse diffusive flux model was done by graduate student Jack Luong.

### 3.1 Experimental Setup and Materials

Three types of experiment were performed in the Applied Mathematics Laboratory. Two of these experiments used a shared set up involving an adjustable acrylic plane. One experiment involved studying the bidisperse case where two particle varieties of a common density but different size were tested. The other involved experiments with a single particle species in the ridged regime. In this regime, the initial particle volume fraction is very high, and particles have a chance of being “shed,” as quasi-solid chunks. The other experiment type involved using a small container to study the phenomena of hindered settling of multiple particles in a fluid. This section provides a detailed discussion of the two cases which involved the plane set up.

The acrylic plane on which experiments were performed includes a 90cm by 14cm track, as well as a 5cm by 14cm reservoir. The mass of the spoon and cup are first measured and recorded to account for the loss of mixture when transferring it from the cup to the track. After, the proper amount of oil and particle masses were separately measured, then mixed together. During mixing, we attempted to reduce the amount of air bubbles introduced by stirring gradually and tapping the cup on the ground every so often.

While this was taking place, we had another person set up the cameras (and laser for analysing height profile). For the front profile tests of the bi disperse and mass shedding cases, ensure the top view camera can see as much of the track as possible, ideally from 10cm to the bottom of the track. For mass shedding, a second camera, such as a GoPro in our case, is used to record the scale to identify the weight of each individual mass shed and the overall mass loss throughout the experiment. Alternatively, if a laser height profile experiment is conducted, we tried to have the side camera as horizontal and parallel to the track as possible, and zoom in on a close range (20cm-30cm) for the most accurate results.

Once ready, the fluid can be poured above the gate at the top of the track and then released from the reservoir at varying amounts by lifting a sliding door. Depending on how viscous the fluid may be, or how steep the inclination angle, it may be necessary to use the spoon to scrape the mixture into the reservoir when it sticks to the gate, and then stir it in the reservoir to prevent it from settling before the gate is lifted. Fold a paper towel in half and using it to catch any left over particles that drip down from the gate can help prevent it from falling on the track and messing with the experiment as you lift it up out of the railing. The cup and spoon are then measured after pouring to calculate the amount of slurry left in the cup, so that the loss of mass can be accounted for in the experiment.

The ramp itself can be adjusted between 10 and 70 degrees in increments of 5 degrees. A reservoir is located below the plane to catch fluid at the end of experiments. A variety of paper colors can be placed inside the plane between its two layers in order to provide a contrasting background for the experimental footage and increase the visibility of particles. Figure 3 shows an image of this set up at an angle of 30 degrees, with the reservoir retracted. A camera can be mounted in one of two configurations - either directly above the plane to observe the behavior of the slurry front - or on the side to observe the height profile of the slurry. A laser is often used when observing the height profile to provide a better outline.

After the experiment is done, the entire track and gate is thoroughly wiped down with paper towels to prepare for the next experiment. Make sure to never use any cleaner on the track itself, as that could introduce differences in the ramp that affects fluid behavior and data collection.

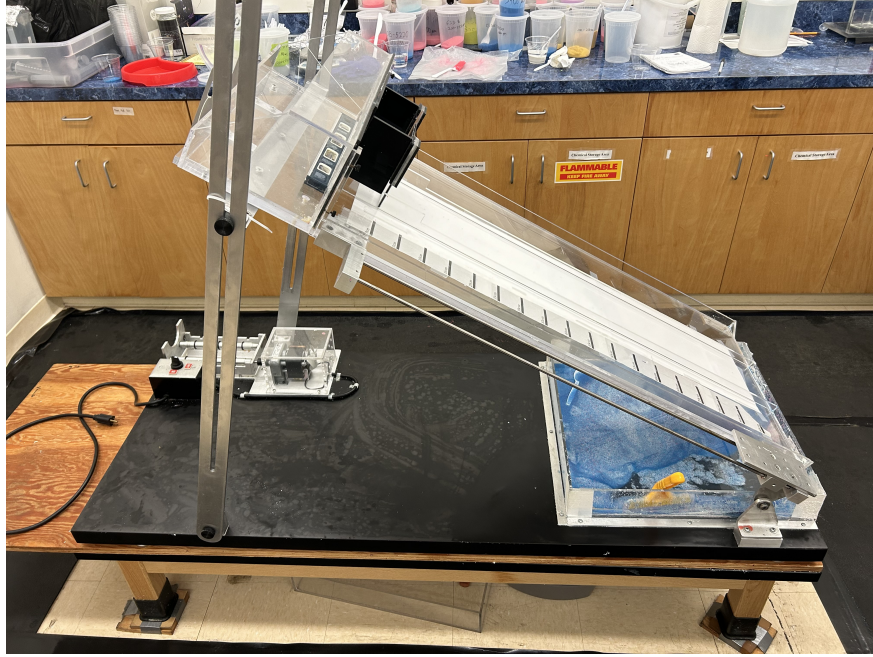


Figure 2: Acrylic ramp setup

Silicon oil with a viscosity of 1000 cSt was utilized for all experiments on involving the acrylic plane. A variety of particles of varying material were used. Table 1 summarizes the properties of the utilized particles. Particles of two material were utilized for the mass shedding test, in order to gain insight into how density affects the behavior of the slurry. Particle species were mixed with a specific volume of silicon oil in order to create a slurry of a particular volume fraction for testing.

Particle Type	Density ( $kg/m^3$ )	Diameter ( $\mu m$ )	Material
GSB-1	2475	850-1700	Glass
GSB-3	2475	450-800	Glass
MIL-5	2475	297-400	Glass
MIL-7	2475	177-250	Glass
GB-5220	2475	200-400	Glass
BSLZ-2	3860	125-250	Ceramic
BSLZ-3	3860	250-425	Ceramic

Table 1: Material properties of particles

Above is the table of all the different particles we used. Particles of different size and densities will give different behaviors, and so we tried to test a wide range of particles for more robust results.

### 3.2 Particle Dyeing and Sieving

A key aspect of successfully performing experiments is to be able to clearly determine the different fronts created by the particles and liquids. Some particles, like the ceramic particles and DB-5220 particles (which are dyed blue), easily stand out against the clear fluid. Glass particles on the other hand, must be dyed to stand out from the fluid. Dyeing is also extremely important to ensure different particle species are distinguishable from each other in the bidisperse case.

In order to dye particles, a mass of 400g of particles were weighed out. Then, 10mL of water and 10mL of the desired paint were mixed together in a beaker until they formed a homogeneous solution. The mass of particles were then added to a bag, followed by the paint/water solution. The bag was then shaken until the paint was evenly spread over, and then were removed from the bag and spread out along either a paper plate or a tray made out of aluminum foil. Particles were spread out and occasionally tilled using a plastic fork in order to maximize surface area exposure to the air. If the particles did not dry quickly, they were either set out in the sun or placed in the microwave oven to quicken the process. After drying, any solid chunks were broken up, and was all added to a bag or deli container for storage. Figure 4 above shows multiple species of particles drying.

The size of the particles was of particular concern for bidisperse experiments. To ensure a narrow size distribution for each particle species involved in the experiment, particles were heavily sieved before being used. Stainless steel food-grade strainer mesh sieves were employed for this purpose. The sieving process involved placing the particles in the mesh sieves and shaking them by hand to allow the smaller particles to pass through while retaining the larger ones. After sieving for a duration of at least one hour, particles were sorted based on their size range (125-400 $\mu\text{m}$ , in increments of 50  $\mu\text{m}$ ). This process was repeated multiple times to achieve a consistent and narrow particle size distribution, which is crucial for the accuracy and reproducibility of the experimental results.



Figure 3: Multiple particle types drying

### 3.3 Mass Shedding

To investigate the mass-shedding phenomenon in gravity-driven particle-laden flows, we conducted a series of experiments using a mixture of particles suspended in a viscous fluid. The experiments aimed to observe the behavior of the particle front as it moved down an inclined plane, particularly focusing on the conditions under which the particle front separates from the bulk fluid and moves as a quasi-solid.

For mass-shedding, research was conducted using the aforementioned adjustable inclined track (Figure

3). Located at the bottom of the apparatus is a thin tray for collecting the shed particle and fluid slurry mixture. A counterweight is placed on top of this tray, which is then placed on top of a zeroed-out scale to record the weight of the mass shed as it falls onto the tray.

The suspension was prepared by mixing particles and a viscous fluid in specific volume fractions, with the particles dyed bright colors to enhance visibility. The inclined plane was set at various angles ranging from  $40^\circ$  to  $65^\circ$  to observe the effects of inclination on mass-shedding. Each experimental run utilized the aforementioned track apparatus, allowing the suspension to flow down the plane. The flow was recorded using a high-resolution camera positioned above the plane, capturing the entire length of the plane, and a separate camera was used to record the mass of each individual shed. The videos were analyzed to track the front positions of the fluid and particles over time, and both the scale and top videos were compared to correlate each mass shed with its corresponding weight. In the end, the time of each shed, its weight, and the distance from the top of the track it shed at was recorded and analysed.

### 3.4 Bidisperse

The bidisperse experiments aimed to investigate the behavior of mixtures containing two distinct particle sizes of the same density as they flowed down the inclined plane to understand how different particle sizes interact and settle within the fluid.

Similar to mass-shedding, the bidisperse experiments were executed utilizing the adjustable inclined track. As opposed to the tray and scale being located at the bottom of the apparatus, there is instead a reservoir for collecting experimental waste.

A mixture of two particle sizes was prepared, with each size fraction dyed differently to distinguish them during analysis. The inclined plane setup used was the same as in the mass-shedding experiments, with angles adjusted to observe the settling behavior of bidisperse mixtures. The suspension was released from the reservoir as in the mass-shedding experiments, and the flow was recorded and analyzed similarly, focusing on the separation and interaction of the two particle sizes.

The procedure for the bidisperse experiments involved preparing the bidisperse suspension by mixing the two particle sizes in the desired ratio. The inclined plane was set at various angles ranging from  $40^\circ$  to  $55^\circ$  to observe the effects of inclination on mass-shedding. Each experimental run utilized the aforementioned track apparatus, allowing the bi-sized suspension to flow down the plane. The flow was recorded using a high-resolution camera positioned above the plane, capturing the entire length of the plane. The recorded videos were analyzed to track the front profiles of both particle sizes and the fluid front, using image processing techniques to enhance visibility.

### 3.5 Numerical Simulations

The equilibrium equations (44a), (44b), and (44c) were solved with a shooting method, and the system of conservation law equations (43a) and (43b) were solved with an upwind scheme. Table 2 shows some of the parameters we used for our simulations. We use a single rectangular pulse for the initial condition as shown in Figure 4.

Table 2: Parameters for numerical simulations

Parameter	$\rho_p$	$\rho_\ell$	$g$	$L$
Value	2475 kg/m <sup>3</sup>	971 kg/m <sup>3</sup>	9.8 m/s <sup>2</sup>	1 m

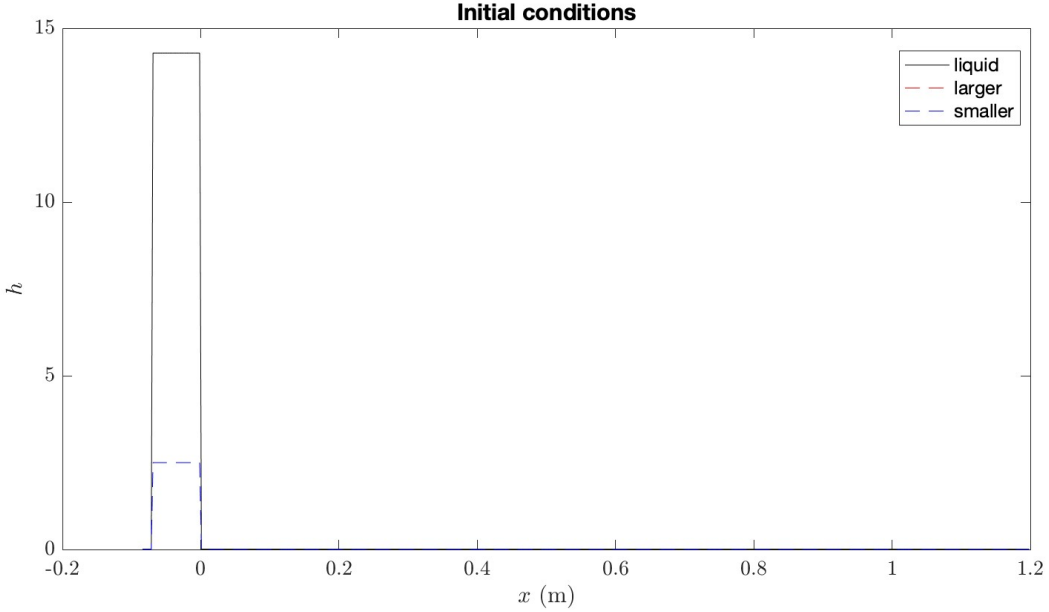


Figure 4: Initial conditions.

## 4 Image Analysis

The general purpose of image analysis for our project is to collect data from the experiments and compare that data to the numerical results developed in previous literature to look for qualitative and quantitative agreement between the two areas. In the following sections we discuss the procedure and results of such image analysis in the bidisperse, mass-shedding, and hindered settling experiments. Each form of processing has a different indicator we use to get a general idea of the movement of the particles and fluid. Any code will be provided upon reasonable request.

### 4.1 Finding the Front Profile

Getting the front profile of the particles is most important in the bidisperse experiment. We are looking for the distance various particle fronts have traveled in order to compare the results to our numerical analysis. The important components for the image analysis is a clear, well-lit video of the particles flowing down the ramp with a clear view of marks every 5 cm which are used for scaling. The background we use is a white paper, but any background of uniform coloring would work.

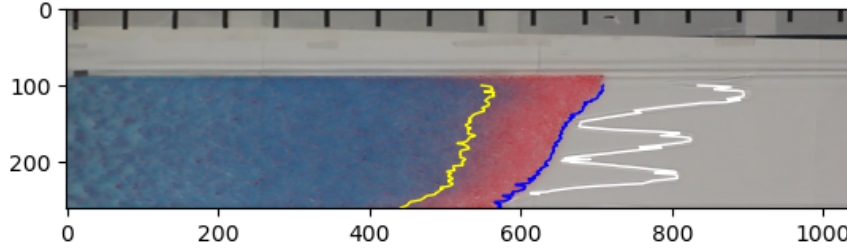


Figure 5: Finding the various fronts. The program marked the liquid front with a white curve and the big and small particle fronts with a blue curve and a yellow curve correspondingly.

To go from our original video to acquiring the particle fronts as seen in Figure 5, we have to first do some preprocessing of the video.

We begin by splitting the video into frames. The original video is around 12 to 15 minutes, so this is important to shrink the file to a workable size. We typically take every 100th frame of the original video. The number of frames taken isn't too important, in our experiments we are typically left with around 300 frames to use in image processing. It is very important to keep track of the FPS the camera originally shot in and how many frames you take from it. This is important to use the correct time step to use for each frame.

```
create_folder() # to hold data

currentframe = 0 # starting number for frame

while(True):
    # reading from frame
    ret,frame = cam.read()
    if ret:
        frame_name = frame + str(currentframe) # come up with good naming convention
        name = './data/' + folder_name + '/frame' + frame_name + '.jpg'

        # writing the extracted images
        frame = frame[:,x_end:x_start]
        cv2.imwrite(name, frame)

        # increment frame counter
        currentframe += 1
    else:
        break

# Release all space and windows once done
cam.release()
cv2.destroyAllWindows()
```

Above shows the code used to create these frames, we import cv2 and os to help with folder and file creation.

Here `cam` is the location of the video we took and `folder_name` is the directory where we are storing our frames. Here we use the naming convention `frame00000.jpg` for the first frame and increment the counter for each successive frame. Using a good naming convention will be critical when starting the next section of preprocessing.

After breaking the video into frames, we have to make sure it is displayed correctly. The image may need to be mirrored or rotated in order for the tic marks to be at the top of the image, and the fluid to be flowing from the left to the right of the frames. After this, we crop the image to the area we are interested in. Selecting the top left and right of the ramp, making sure to include at least a little part of the marks. The bottom left and right of the ramp should only just show the bottom the fluid. Finally, we must note the y coordinate where the fluid begins. In Figure 5 that would be about 100.

The first time collecting these parameters, the user will be able to select various points to get a good selection without having to guess at various coordinates. On any further runs of the code, since certain parameters like threshold will have to be adjusted many times to get an optimal processing, the parameters will be kept in a config file to be able to quickly acquire them and allow for identical runs where only the parameters chosen are changed.

The flipping and rotating is relatively easy to do, and one of the quicker parts of processing. Below, the code we use for these transformations is seen, where at each step, a boolean value decides if the transformation is applied.

```
# Apply transformations to image
if rotate:
    new_im = np.zeros((imgs.shape[0], imgs.shape[2], imgs.shape[1], imgs.shape[3]))
    for i in range(imgs.shape[0]):
        new_im[i] = np.transpose(imgs[i], (1, 0, 2))
    imgs = new_im
if x_flip:
    imgs = imgs[:, :, ::-1]
if y_flip:
    imgs = imgs[:, ::-1, :]
if rescale:
    imgs = imgs / 255
imgs = imgs[:-2, :, 30:]
```

The final transformation is a projection, which uses our selection of the corners to show only the area we are interested in for the ramp. The code is too long to include here (again the code can be made available upon reasonable request), but from Figure 6, it is clear how we get to the final images we will use in image processing from the rotated/flipped images using the corners selected.

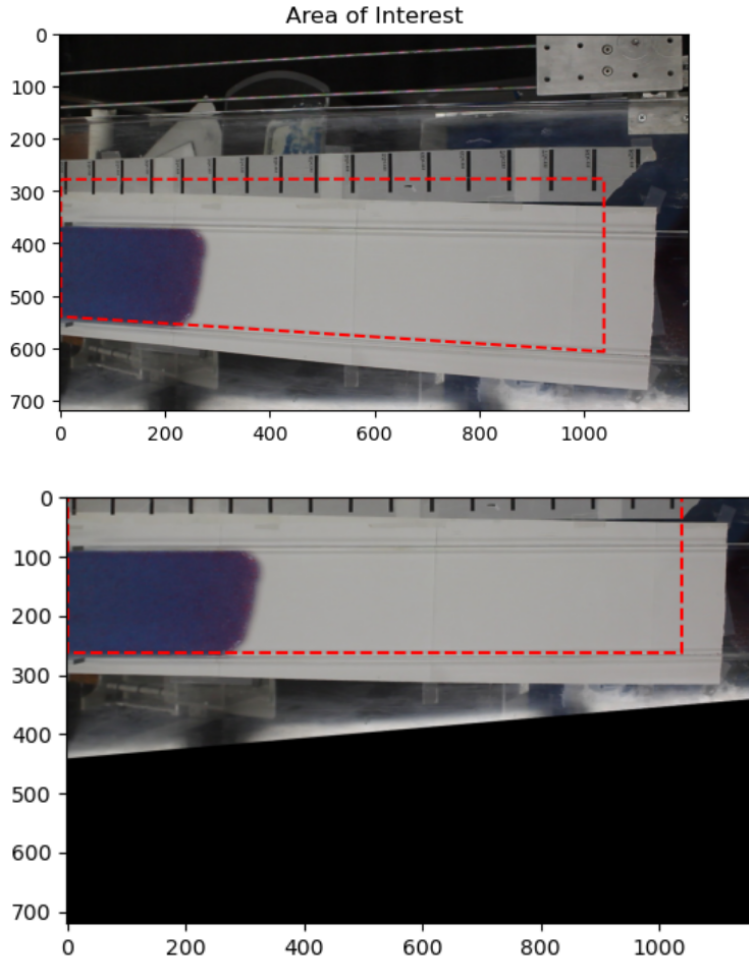


Figure 6: Example of selecting the area of interest

The red dotted line shows the final selection of our image. This is the area we will be using image processing on.

There are many ways to go about processing these images. For this particular run, we find the hue of the two different particles by averaging hue over areas where the particles are clear and separated. These hues are used, along with a given threshold to find the particle fronts.

```
# Defines the particle color to be used in boundary detection

color = np.mean(imgs[c_ind] [y_start:, c_start:c_end], axis=(0, 1))

if c_start_2 != -1:
    color2 = np.mean(imgs[c_ind_2] [y_start:, c_start_2:c_end_2], axis=(0, 1))
else:
    color2 = color

background = imgs[0]
```

By taking the mean of a specified area, we get a value for the color that we are interested in tracking. Again, for this case, we are finding the second particle front using a similar method, defining an alternative area to find the color. Alternatively, we could have used the same color but defined a different threshold if the different particles were closer in color.

```
# Displays particle and fluid fronts for sample image

ind = 47

temp_thresh = thresh_particle + (THRESH_STEP * ind)
temp_thresh_2 = thresh_particle_2 + (THRESH_STEP * ind)
print(imgs[ind].shape)

n_img = imgs[ind] - background
n_img[n_img < 0] = 0

marks = get_tics(imgs[ind], 0, mark_y_end, mark_x_start, tic_thresh, plot = True)

a, b, mask = get_particle_bound(imgs[ind], color, temp_thresh, y_start)
_, _ = get_fluid_bound(n_img, y_start, mask, org_img=imgs[ind])

if thresh_particle_2 != -1:
    a2, b2, mask2 = get_particle_bound(imgs[ind], color2, temp_thresh_2, y_start)
```

In this section of the code, we can test various thresholds to make sure we are getting correct detection of the various boundaries. We can scan over different indices to verify the boundary detection, the main parameters that will need to be changed are `thresh_particle` and `thresh_particle_2` in order find the best thresholding for edge detection.

Along the y-axis, we select the right-most pixel that exceeds this threshold as the point for our particle front. The fluid front can be found by taking the pixel with the lowest gray-scale value right of the particle front, this works well since the fluid front casts a shadow that is easily picked up through this process.

Once we are satisfied with how the edge is being found, we look at perform the edge detection on all frames. A graph such as Figure 7 can be displayed to again ensure our data looks reliable.

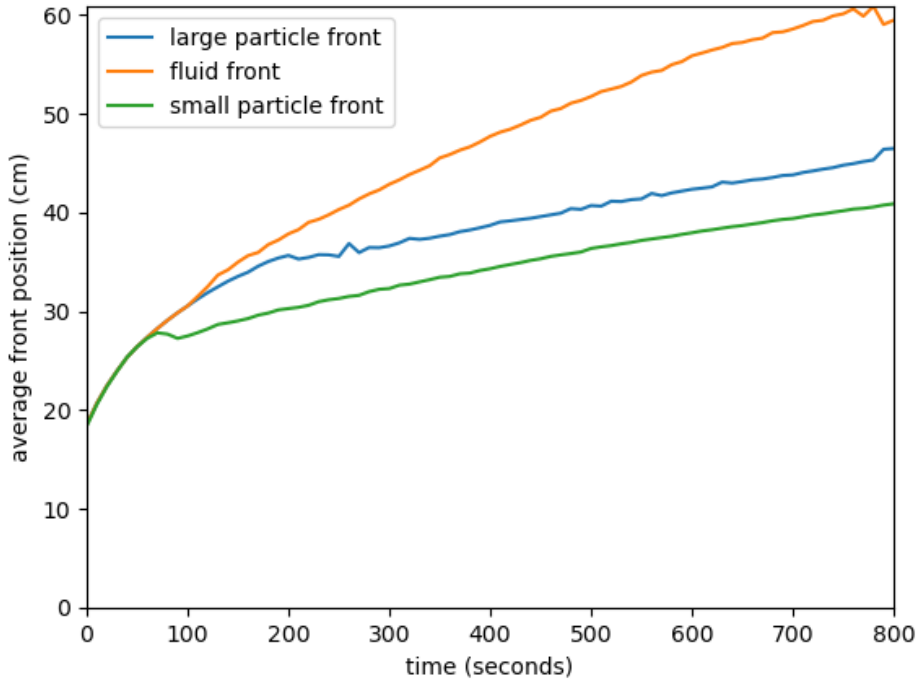


Figure 7: An example of the particle fronts

A final section outputs the front data as a bin file and a matlab file which can be used in a comparison with our numerical analysis of what should happen given the parameters we are working with. Thus we are able to extract data from our experiments that can be compared to the theory behind bidisperse particle laden flow in order to inform us on how our model can be improved and hopefully lead to a more realistic model that agrees with experimental results.

## 4.2 Laser Height Profile

The laser height profile is important to analyse, especially for the mass shedding case. The goal behind these experiments is to determine the ridged particle height that occurs the moment before the mass sheds. This could allow us to compare experimental data to literature discussing a critical height attributing to iceberg calving [3].

The experimental setup for the laser height profile is mentioned generally under the Experimental Setup and Materials section. To specifically adjust the laser line, let the slurry fall down the track for a little bit and set up the laser in line with where you are most likely to see shedding occur. We make sure to set up the camera lower in the ramp where shedding occurs. This is typically from the 30cm to 85cm region. It is recommended to get a narrower length, though, as it prevent problems with the precision of the calibration to determine the pixels per inch of each frame. On top of this, making sure the camera was flush with the track made image processing easier to have a straight horizontal line in compared to a diagonal one.

At the start of this project, the preexisting laser height profile python code did not work with our experimental setup, and so we rewrote most of it.

```
# Loop through images and resize them
for i in range(im_start, im_end + 1, im_step):
```

```

img_path = image_prefix + dec.format(i) + image_suffix
try:
    with Image.open(img_path) as img:
        img_resized = img.resize(resize_dims, resample=Image.LANCZOS) # or Image.BILINEAR
        resized_img_path = resized_dir + dec.format(i) + image_suffix
        img_resized.save(resized_img_path)
        print(f"Saved resized image: {resized_img_path}")
except FileNotFoundError:
    print(f"Image {img_path} not found.")
except Exception as e:
    print(f"Error processing image {img_path}: {e}")

print("Finished resizing images.")

```

Here, the code was rewritten to resize the images so that our computers could handle the image processing. Before, the videos were filmed in 4k and it caused our computers to crash, or take forever to store. This will re save the images in 720p or any resolution manually inputted to solve this solution.

The images are then analysed so that we select a specific section of the image that contains all the information necessary to analyse, then threshold it to observe the height of the laser from a zeroed position that has been calibrated. The code below shows the selection process of the frames.

```

h_img = imgs.shape[1]

area_of_interest = [(x1, 0),
                    (x1+h, 0),
                    (x2+h, h_img),
                    (x2, h_img)]

area_of_projection = [(0, 0),
                      (0, h),
                      (h_img, h),
                      (h_img, 0)]

project_planes(imgs[5], area_of_interest, area_of_projection)
_ = project_transform(imgs[5], area_of_interest, area_of_projection, plot=True)

# Displays description of image transformation to get correct orientation
def project_planes(image, src, dst):
    x_src = [val[0] for val in src] + [src[0][0]]
    y_src = [val[1] for val in src] + [src[0][1]]
    x_dst = [val[0] for val in dst] + [dst[0][0]]
    y_dst = [val[1] for val in dst] + [dst[0][1]]

    fig, ax = plt.subplots(1,2, figsize=(13,6))

```

```

new_image = image.copy()
projection = np.zeros_like(new_image)
ax[0].imshow(new_image)
ax[0].plot(x_src, y_src, 'r--')
ax[0].set_title('Area of Interest')
ax[1].imshow(projection)
ax[1].plot(x_dst, y_dst, 'r--')
ax[1].set_title('Area of Projection')
plt.plot()

def project_transform(image, src, dst, plot=False):
    x_dst = [val[0] for val in dst] + [dst[0][0]]
    y_dst = [val[1] for val in dst] + [dst[0][1]]

    tform = transform.estimate_transform('projective',
                                         np.array(src),
                                         np.array(dst))
    transformed = transform.warp(image, tform.inverse)
    print(dst[0])
    if plot:
        plt.figure(figsize=(6,6))
        plt.imshow(transformed[:dst[1][1], :dst[2][0]])
        # plt.plot(x_dst, y_dst, 'r--')
    return transformed

```

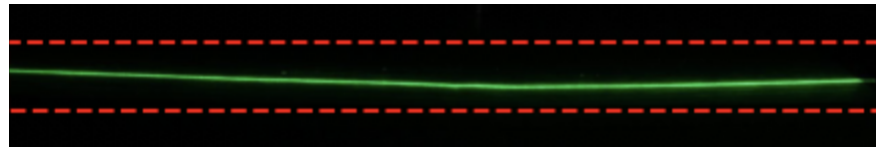


Figure 8: The manually selected box around the area of relevant height profile

As seen from the image, the laser height has a curve in the center due to it reflecting off the paper, which was not flush with the ramp, but sagging downwards. This, along with taking too wide a length of data, and poor calibration shots, lead to issues in analysing the laser height profile. It created coherent height profiles near the start, but then soon digressed into indistinguishable noise and distorted shapes that did not look nearly like the laser height in the individual frames.

The data from the experiments is not worth nothing due to the aforementioned issues, and further talks on how to improve the experiment are discussed later in the report in Section 7.1.

## 5 Results

### 5.1 Bidisperse

#### 5.1.1 Front Profile

We compared the simulation results to our experimental data. The results are shown below in Figure 9.

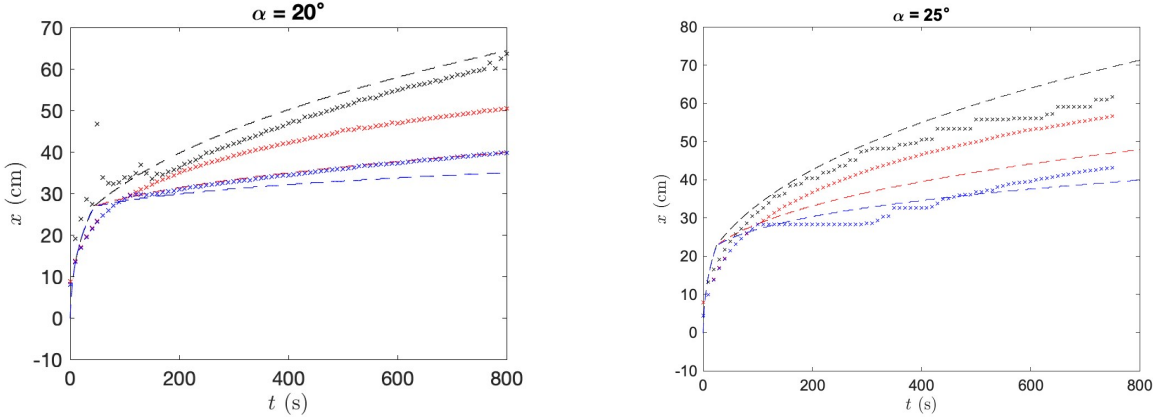


Figure 9: Front positions for the bidisperse system with fixed volume initial conditions for angles  $\alpha = 20, 25$  deg. The larger particles are GSB-3 particles with  $600\text{--}800 \mu\text{m}$  diameters, and the smaller particles are DB-5220 particles with  $300\text{--}355 \mu\text{m}$  diameters. The black, red, and blue curves represent the front positions over time of liquid, bigger particles, and smaller particles correspondingly. The dotted lines are experimental data and the dashed lines are numerical solutions.

The model correctly predicts the separation of the particle fronts and the liquid front that we observed in the experiment. However, the simulation currently predicts a smaller separation of the particle fronts than what we observed in our experiment. One potential issue is that the current flux function, the empirical tracer flux in particular, is not optimal. This issue can be solved by experimentally determine a better flux function. Another potential issue is the inaccuracy in determining the front location of the smaller particles. As shown in Figure 10 (also predicted by our simulation in Figure 11), there is a layer of pink particles in the region where the blue particles emerge, which causes this inaccuracy. Also, due to the asymmetry of the slurry in the transverse direction (see Figure 12), which is caused by differences in shear stress, the averaged front may not be the best statistical quantity to compare with simulations. For our future experiments, we will improve image processing to better determine the particle front locations and experimental techniques to reduce asymmetry in slurry flows. We will also look into other statistical quantities (e.g. median) to compare with simulations.

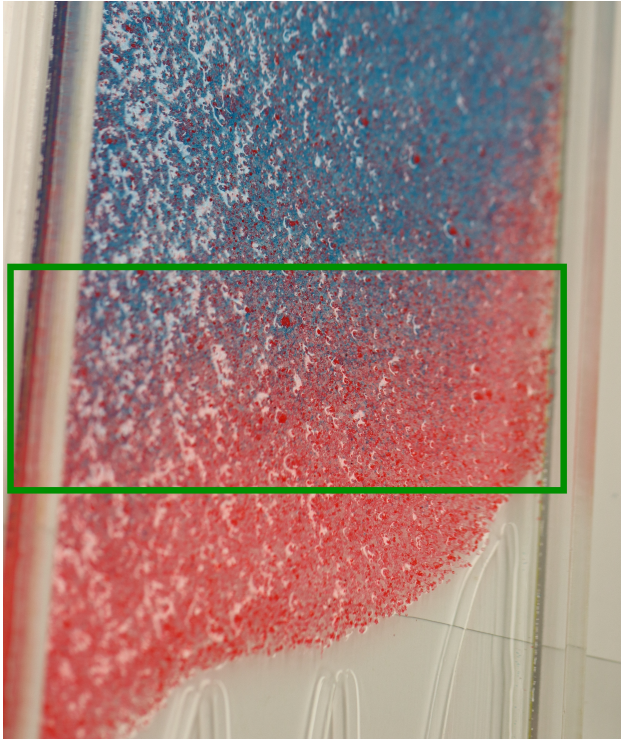


Figure 10: Overlap of particle layers. The green box shows the region where the overlap happens.

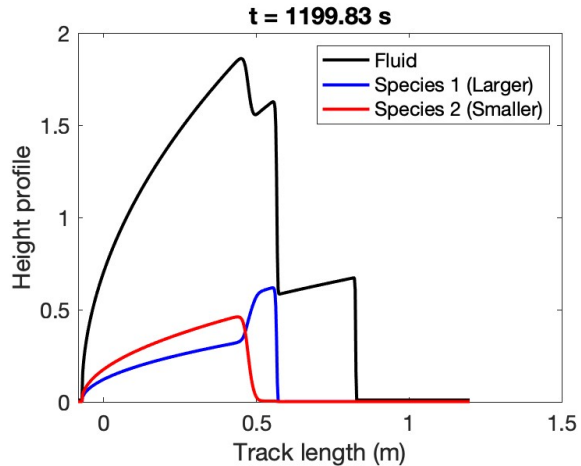


Figure 11: Example simulation plot. The simulation predicts a region of overlap of the particle layers similar to what was observed in the experiments.

### 5.1.2 Spiral Separator

As a side note from the bidisperse experiments, our group decided to try and make our own spiral separator to observe the phenomena we see in mining applications, where heavier particles settle out from the lighter ones. We used Lingyun Ding, Sarah Burnett, and Andrea L. Bertozzi's unpublished paper on "Equilibrium theory of bidensity particle-laden suspensions in thin-film flow down a spiral separator" to guide the design

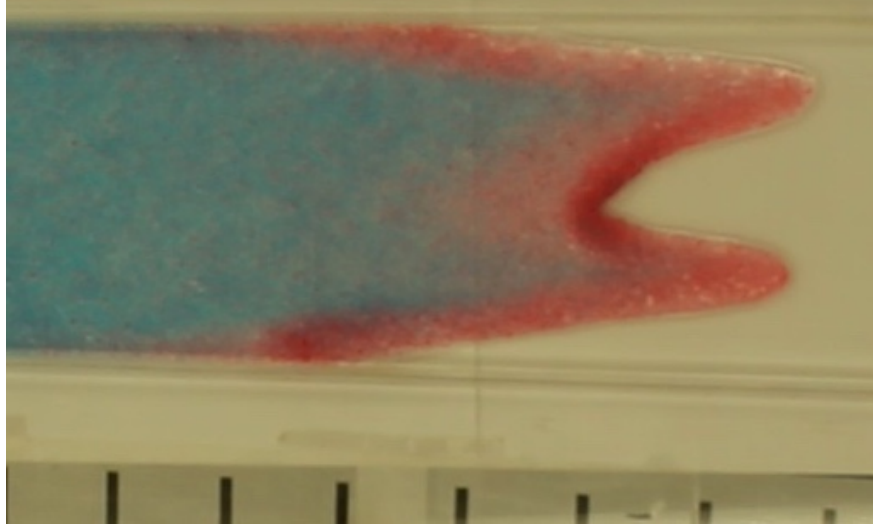


Figure 12: Flow asymmetry. This is an experiment done at  $\text{ang} = 30^\circ$  with  $\phi = 0.35$ . The particles on the two sides of the slurry had already started to settle but the middle part of the slurry remained ridged.

of our own replica. To begin with, we used Solidworks Computer Aided Design software to model our own spiral separator, and then print it out to obtain experimental results.

To print it, we used a 0.3 layer height, 15% infill, tree supports, and scaled the full sized model down to make it quicker and easier to print prototypes. We were able to print two different versions of the small scaled model, with the second one improving on the first by more snugly fitting the separators to each other.

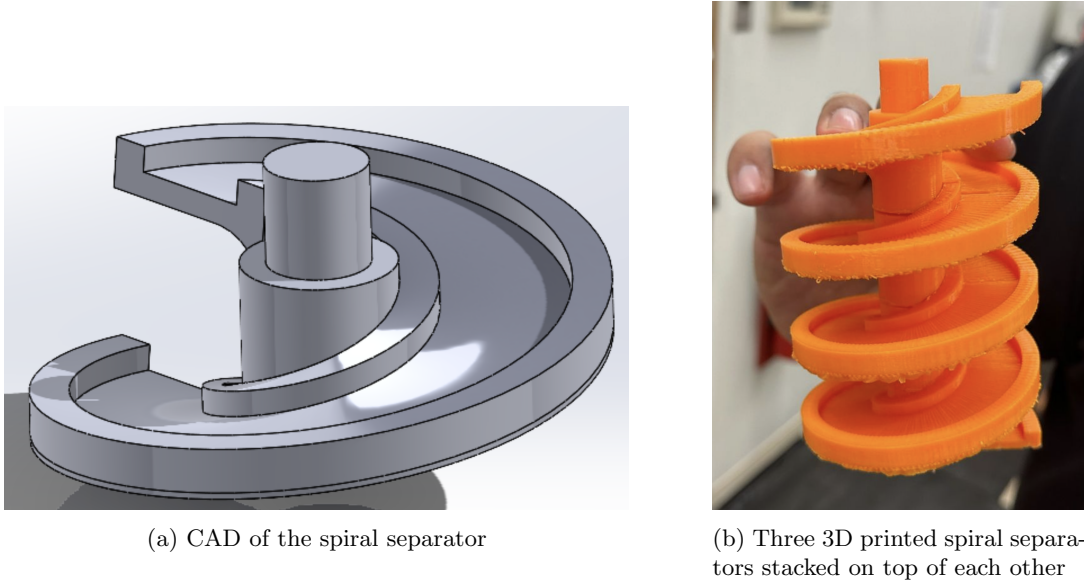


Figure 13: Comparison of the CAD model and the 3D printed spirals.

They were designed by having the spiral rotate around the base a full  $360^\circ$ , with a nub on the top and hole on the bottom to connect multiple spirals together like Lego pieces. This allows control for the length of the separator, and modularity in case one of the separators breaks and needs to be replaced. Two issues were in place. One is that the roughness of the surface due to the 3D printing method introduced another

variable that needs to be controlled for, and the small size created flow separation in the inner radius of the spiral as the fluid fell down it. These solutions can be fixed by printing with a smaller layer height, using post processing methods such as sanding to smooth down the surface, and printing a larger spiral.

A larger spiral was attempted to be printed, but issues with the printer caused it to fail and is something that can be revisited in the future.

## 5.2 Mass-Shedding

Here we present the results of our mass-shedding experiments. Through all the experiments, we control for the particle volume fraction,  $\phi$ , the inclination angle,  $\alpha$ , and compare them for two different particle densities using ceramic and glass particles of similar sizes. The results of both ceramic and glass particles is presented respectively below. An error was found in one of the sheets used for volume fraction calculations, leading to a discrepancy between the desired volume fraction, and actual volume fraction of the mixtures for the ceramic particles. The actual fraction after the error was accounted for is in parenthesis.

$\phi$	0.3 (0.297)	0.35 (0.347)	0.4 (0.396)	0.45 (0.446)	0.5 (0.496)	0.55 (0.546)
55°	No Shed	3g Shed	22.2g	14.5g Shed	11.6g Shed	Large shedding immediately
65°	2g Shed	6.8g Shed	14.2g Shed	27g Shed	35.5g Shed	Unstable, heavy shedding

Table 3: BSLZ-3 Total Mass Shed ( $\rho = 3860 \text{ kg/m}^3$ )

$\phi$	0.3	0.35	0.4	0.45	0.5	0.55
55°	5.5g Shed	11.6g Shed	19g	Instant Shed	Instant Shed	N/A
65°	12.8g Shed	17.8g Shed	23.5g Shed	Instant Shed	N/A	N/A

Table 4: MIL-5 Total Mass Shed ( $\rho = 2475 \text{ kg/m}^3$ )

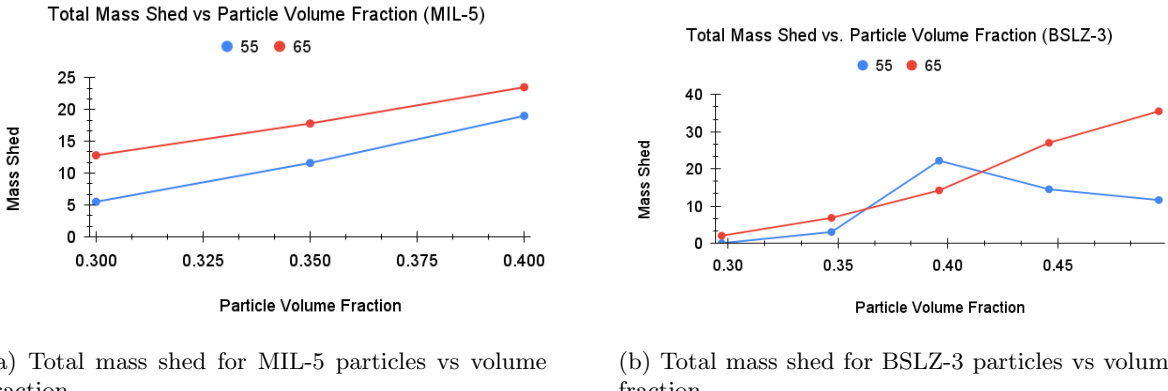


Figure 14: Comparison of total mass shed for MIL-5 glass and BSLZ-3 ceramic particles as particle volume fraction increases over time.

Here, we see the general trend that as the particle volume fraction increases over time for a fixed inclination angle, the total mass shed also increases. One interesting behavior to note is the contradiction to this trend with the ceramic's trend line for  $\alpha = 55^\circ$ . One explanation for this deviation are issues with our experimental procedure. The track has a finite length, and so there might not be enough time for the mass to entirely

shed at higher volume fractions in the given length, resulting in a decrease in total mass loss past a certain point.

In addition, the lack of data points for the MIL-5 glass particles can be attributed to the small range at which mass shedding occurs at these inclination angles. Past a certain angle and volume fraction, the slurry enters a new instant shedding regime, where the bulk motion of the mixture acts as a quasi-solid and all instantly falls to the bottom of the track, similar to how a solid would accelerate downwards. On the contrary, the opposite phenomena occurs at low volume fractions and inclination angles, where there is a distinct ridged particle front, but no shedding at all. Here, the particles are unable to clump enough to break off and fall down the track, although there would be potential for shedding to occur under a much longer time scale.

The following graphs provide examples of the kind of data and information that can be gleaned from individual trials. During experiments, data collection focused on tracking how large each mass was shed, and where in time and space it was shed. From these measurements, multiple graphs can be constructed that give insight into the details of the mass shedding problem.

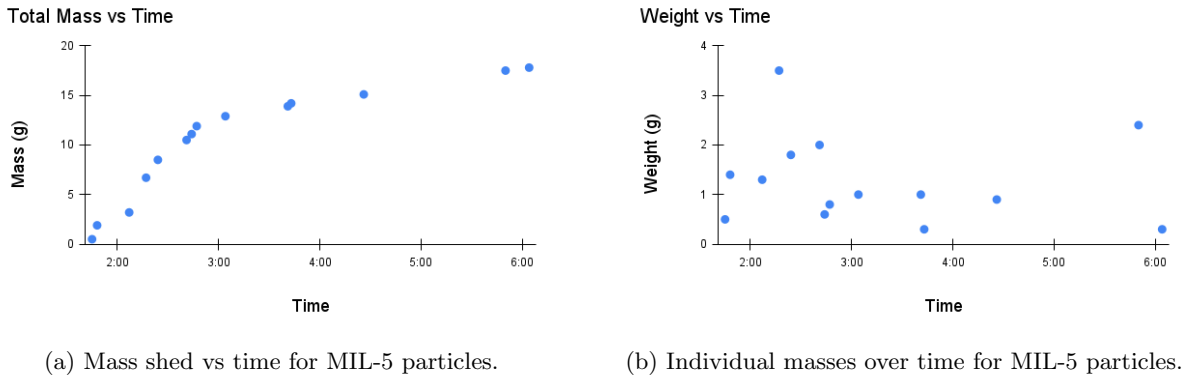
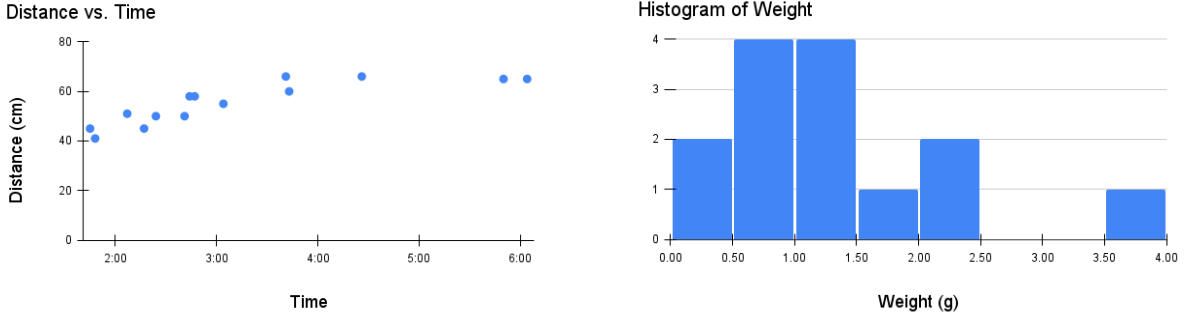


Figure 15: Mass shed analysis over time for MIL-5 particles.  $\alpha = 65^\circ$  and  $\phi = 0.35$

Figure 15a, which shows a plot of the total mass shed over time, shows that the majority of mass is shed in the beginning of an experiment. Over time, mass is shed less often and in smaller amounts. This trend seems to occur in the broad majority of tests performed, and makes sense given a constant volume experiment, where the net volume of particles decreases as they shed off over time. Figure 15b complements the former figure as well, and shows the weight of each shed over time. This graph shows that larger masses tend to be shed in the beginning, except for the occasional large shed near the end - which can be seen as an outlier.

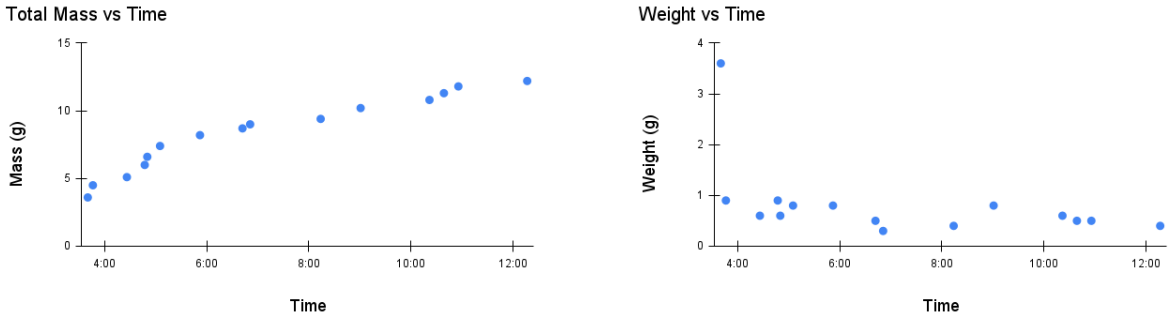


(a) Distance shed over time for MIL-5 particles.

(b) Histogram of the weight of sheds for MIL-5 particles.

Figure 16: Distance and individual weight of mass sheds analysis.  $\alpha = 65^\circ$  and  $\phi = 0.35$

Figure 16a shows the distance each shed occurs with the corresponding time of shedding. This shows when shedding first begins for a test - and also indicates that as time progresses, more masses seem to be shed from the same position. This tracks with the observation that as the experiment progresses - the front speed slows down greatly. After looking at many different trials, there also seems to be distinct "hot spots" along the length of the track where the masses shed, showing a dependence on the distance traveled to when it will shed. The fingers will shed at said length first, then once the bulk slurry reaches that same distance at a later time, it will then shed as well. The front movement is further hindered by shedding at the front, which moves the end of the front back with each shed. In certain tests these effects can create a situation where the front moves extremely slowly, while shedding still occurs, keeping the front stuck in the same position. Figure 16b shows a histogram of the mass of each shed. The histogram clearly shows that masses tend to cluster around the lower end of weights, with a few outliers being larger. Generally, the largest shedding occurs near the beginning - but not necessarily first. This makes sense based on intuition, as at the beginning of the experiment the slurry contains a higher number of particles than later on. The next four figures show the same graphs, but for a test with the ceramic BSLZ-3 particles as well.



(a) Mass shed over time for BSLZ-3 particles.

(b) Individual masses over time for BSLZ-3 particles.

Figure 17: Total mass shed and individual masses over time for BSLZ-3 particles.  $\alpha = 55^\circ$  and  $\phi = 0.40$

Figure 17a shows similar behavior to the glass case, where more mass seems to be shed in the beginning of a trial. However, it appears the ceramic tests have more consistent shedding near the end of a trial. This may just be a result of the specific tests performed - and should be verified with further experiments.

Figure 17b agrees with the glass case in that the graph shows that larger masses tend to be shed in the beginning. However, it is clear from this graph that the largest shed for this trial was the first one. From our experiments it appears that the largest shed is more often the very first shed in the case of ceramic than in the glass case.

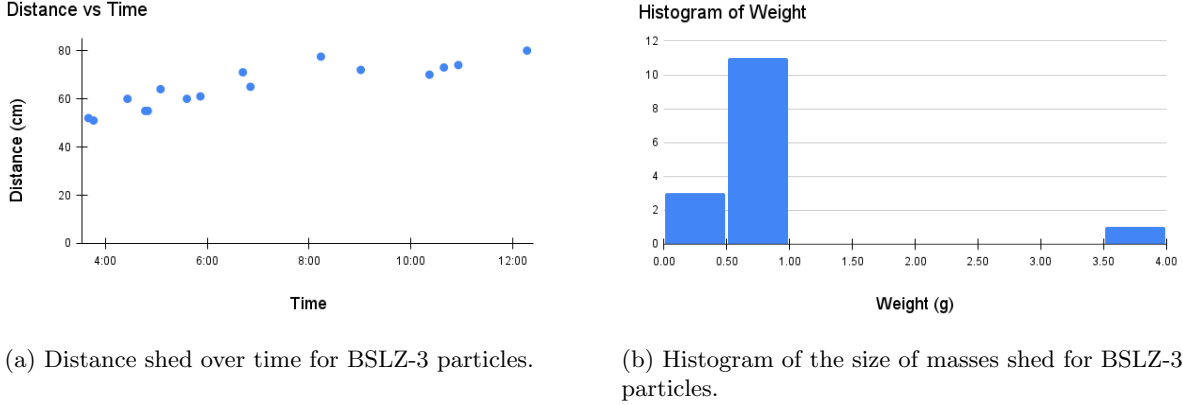


Figure 18: Distance shed over time and the size of masses shed for BSLZ-3 particles.  $\alpha = 55^\circ$  and  $\phi = 0.40$

Like with the glass trial, Figure 18a shows the distance each shed occurs with the corresponding time of shedding. This can also be used to find where shedding first occurs, and also indicates that as time progresses, more masses seem to be shed from the same position. Figure 18b shows a histogram of the mass of each shed. From this histogram, as well as the data from other ceramic tests, it appears that the individual sheds for ceramic tests tend to be less than 1 gram, and are often smaller than the sheds associated with a glass test. The outlier on the right is the initial shed, which tracks with the observation that the first shed is often the largest with the ceramic tests. Despite having smaller sheds, the quantity of sheds tends to be a lot higher for ceramic tests, implying it is easier for the denser particles to break off the bulk fluid motion, whereas the glass need time to accumulate large masses before breaking off.

Outside of the previously discussed array of tests, mass shedding experiments were also performed with other particle types. Numerous experiments were performed with the BSLZ-2 particles. These particles are composed of the same material as the BSLZ-3 particles, and thus have the same density, but fall under the size range of 125-250 microns. Tests were performed at an angle of 55 degrees, with volume fractions of 0.45, 0.5, and 0.55. No test shed any mass - despite appearing extremely ridged and close to shedding at higher volume fractions. A test was also performed at the higher angle of 65 degrees, with a fraction of 0.5, and no mass was shed once again. This indicates a clear dependence on the size of particles - which should be studied further in the future.

## 6 Hindered-Settling

In the bidisperse particle laden flow experiment, many values are found empirically. One example of this is the hindered-settling flux function which is a large contributor to the overall flux function. We believe that this area of the model can be improved, so we aim to collect data in this area to improve our overall model for bidisperse particle laden flow.

There appears to only be experiments for mono-disperse hindered settling [4], therefore we tried to see

if we could set up an experiment well enough to measure bidisperse hindered settling. We hope to find effects that may be unforeseen when including particles from two different species in this hindered settling experiment. These unforeseen effects could contribute to effects in the particle laden flow settling that have so far been neglected.

## 6.1 Background

In this section, we detail the background behind the hindered settling of particles in a fluid. We start with understanding the physics behind the settling of particles. For the case of a single particle settling in a fluid, the forces acting on the particle include buoyancy, gravity, and drag.

$$F_D = 6\pi\eta rv, \quad (47)$$

$$F_B = \frac{4}{3}\pi r^3 \rho_l g, \quad (48)$$

$$F_G = \frac{4}{3}\pi r^3 \rho_p g. \quad (49)$$

Where  $\eta$  is the fluid dynamic viscosity,  $r$  is the particle radius,  $\rho_l$  and  $\rho_p$  are the densities of the fluid and particle respectively, and  $g$  is the acceleration due to gravity. With these equations, we can calculate the terminal velocity, also known as the Stokes speed (which occurs when the velocity of the particle becomes constant). Thus we balance the forces acting on the particle, described by equations (47), (48), and (49) in order to solve for the terminal velocity of the particle given by

$$v_s = \frac{2(\rho_p - \rho_l)gr^2}{9\eta}. \quad (50)$$

This is the maximum velocity that a single particle can settle at, but as more particles are added, this terminal velocity will decrease. This is due to the many particles' interactions with each other and the fluid, hindering the settling speed of all the particles. Because of the large quantity of interactions, it is near impossible to derive the motion of every particle from first principles, and so we resort to deriving a settling function empirically. As a general observation, these functions depend on  $\phi$ , the particle volume fraction, where at  $\phi = 0$ , the settling velocity reaches a maximum of Stokes speed until it reaches a 'maximum packing'  $\phi_m$  where the particle has fully settled.

Currently, there are a variety of hindered settling functions that have already been fitted for the monodisperse case [12].

(a) 'Einstein.' [5]

$$\mu(\tilde{\phi}) = \left(1 + \frac{5}{2}\tilde{\phi}\right) \quad (51)$$

(b) 'Acrivos and Leighton.' [1]

$$\mu(\tilde{\phi}) = \left(1 + \frac{1}{2} \frac{\eta\tilde{\phi}}{1 - \frac{\tilde{\phi}}{\phi_m}}\right)^2. \quad (52)$$

Leighton and Acrivos used this with parameters  $\eta = 0.3$ ,  $\phi_m = 0.58$ ,  $K_c = 0.41$ , and  $K_v = 0.61$  for Couette particle laden flows.

(c) ‘Philips *et al.*’ [13]

$$\mu(\tilde{\phi}) = \left(1 - \frac{\tilde{\phi}}{\phi_m}\right)^{-\psi}. \quad (53)$$

Philips used this hindered settling function where  $\phi_m = 0.68$ ,  $\psi = 1.82$ ,  $K_c = 0.41$ , and  $K_v = 0.62$  for Couette particle laden flows.

(d) ‘Merhi *et al.*’ uses the same hindered settling function with slightly different parameters from suspensions in Couette flow.  $\phi_m = 0.68$ ,  $\psi = 1.82$ ,  $K_c = 0.105$ , and  $K_v = 0.525$ . [10]

(e) ‘Murisic *et al.*’ takes on the same structure with different values from  $\psi$  and  $\phi_m$  compared to Philips.  $\phi_m = 0.61$ ,  $\psi = 2$ ,  $K_c = 0.41$ , and  $K_v = 0.62$  [12]

We use these formulas as a base reference for creating our own hindered settling function, and can be used to see how our own function holds up to the existing literature and experimental data. Note that Einstein’s hindrance function only works well in the dilute limit, where  $\phi$  is sufficiently small, but the other three predict very similar results where the fluid fronts exhibit a  $t^{\frac{1}{3}}$  Huppert-like behavior.

It should be noted these assumptions only hold at a low Reynold’s number ( $Re$ )

$$Re = \frac{\rho_f v_s r}{\eta}. \quad (54)$$

The Péclet number ( $Pe$ ) has also been found to be important from [4]. As there appear to be a crossover  $Pe$  ( $Pe_c \approx 10^8$ ) where the particles transition from Brownian motion to non-Brownian motion, where  $Pe$  is given by

$$Pe = \frac{v_s r}{D_0}. \quad (55)$$

Here the term  $D_0$  is defined as the single-particle diffusivity

$$D_0 = \frac{k_B T}{6\pi\eta r}$$

where  $k_B$  is defined as the Boltzmann constant,  $k_B = 1.380649 \times 10^{23}$  joules per kelvin, and  $T$  is temperature in kelvin.

### 6.1.1 Single Particle

The goal of this experiment was to determine how accurately the predicted Stokes speed of a particle falling, given the necessary parameters, lined up with the experimentally found Stokes speed of the particle.

Initially, we chose parameters such that the time length of our experiment was reasonable. We wanted to analyze the particles falling at Stokes speed, and remove the transient. The transient is a short period of time where the particle is accelerating from rest to Stokes speed. We could then set up an ODE and solve for an analytical solution using integrating factors to then determine the time scale for the transient regime.

$$6\pi\eta rv + \frac{4}{3}\pi r^3 \rho_{lg} - \frac{4}{3}\pi r^3 \rho_{pg} = mv. \quad (56)$$

After solving the equation for our particle sizes and densities, with an initial condition of the particle being at rest, the transient came to be around  $O(10^{-8})$  seconds, and so this was neglected when experimentally

verifying the Stokes speed. The experimental procedure is outlined in Section 6.2 and the image processing and results are given in Section 6.3.

While we haven't achieved the high accuracy in our Stokes speed experiments that we were hoping for, this was a good exercise to have conducted and hopefully improved the parameters we are working with. With more accurate measurements, we will be able to better adjust our model with experimental results. This will also be critical in ensuring our further experiments in hindered settling are accurate and provide useful results.

### 6.1.2 Monodisperse Settling

A base understanding of hindered settling can be gotten from [4]. From the many different results reported and various possible hindered settling functions, we hoped to ensure our experimental setup aligned well with this previous research. However, there was not enough time during this project to pursue this any further. For future groups, it will be good to make sure experimental results align well with these past results before continuing forward. This will ensure there is no confounding variables in the experimental setup creating unwanted or unaccounted effects.

### 6.1.3 Bidisperse Settling

While the monodisperse settling experiment wasn't able to be completed, a bidisperse experiment was still considered important to continue forward with. The goal of this experiment is to get qualitative data on the settling of two species of particles in a viscous liquid. For specifics on the experimental procedure and parameters see Section 6.2. The general idea was to have a jar of well mixed particles coming from two size ranges that could be easily identified so that we could notice which particles are settling closer to the bottom and which settle closer to the top.

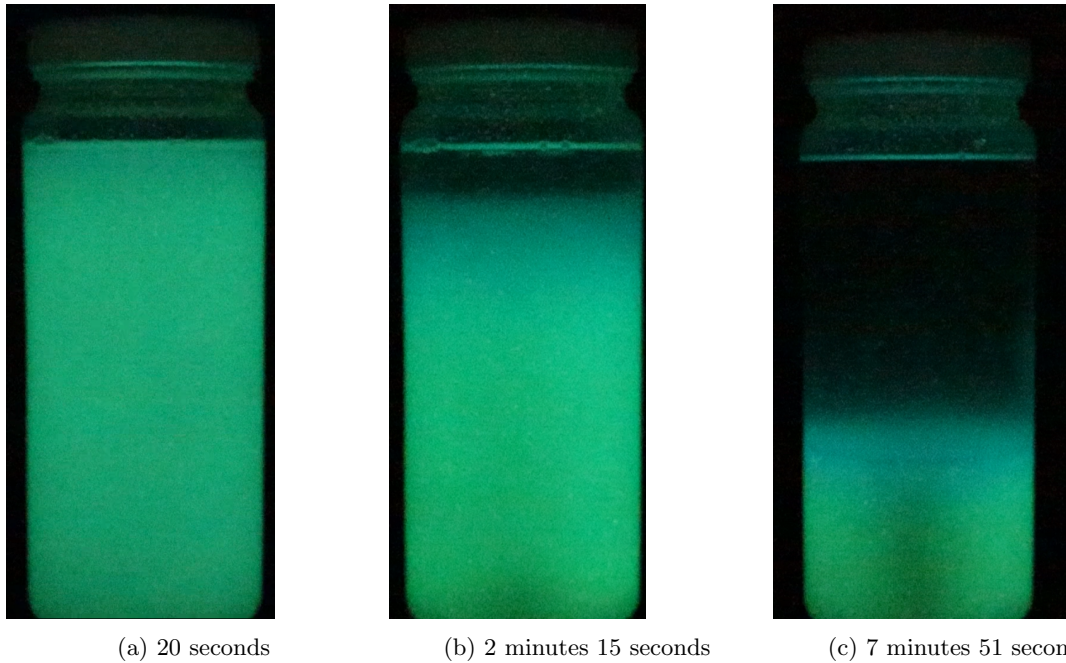


Figure 19: Bidisperse Hindered Settling Experiment

As can be seen from Figure 19, the particles started out well mixed, but as quickly as 2 minutes 15 seconds into the experiment some separation can be seen as the smaller blue particles take longer to settle and the larger green particles can be seen settling more quickly to the bottom. It becomes even more clear when the particles eventually settle that the larger particles were able to settle at the bottom and the blue smaller ones settled on top of these particles.

There was a reasonable explanation for why either particle would settle first. The larger particles have larger radii, so therefore they each would have a faster Stokes speed, hence it would be reasonable to assume the larger particles would be hindered less and settle quicker. Alternatively, we have been considering the Brazil nut effect (granular convection) in many other experiments, so it would not have been too surprising to see the smaller particles settle at the bottom due to this phenomena.

We believe that if given a higher particle fraction, this Brazil nut effect might play a larger role in the settling. Due to this more dilute solution, the larger particles, with a larger Stokes speed, were able to settle quicker. It may also be necessary for some sheer forces perpendicular to the vertical direction to be applied in order for the Brazil nut effect to have an impact on the settling.

In [4], the hindered settling function can be seen to be effected by the Péclet number. This is presumed to be due to the effects of Brownian vs. non-Brownian motion. It would be particularly interesting to see how particles in these different systems interact. From this previous research, the crossover Péclet number is around  $10^8$  and special care should be taken to note which system particular particles lie in when doing various experiments as the crossover from Brownian and non-Brownian motion of particles could play a critical roll in the behaviours of these experiments.

## 6.2 Experimental Procedure

This section looks into the experimental procedure so further experiments can be replicated. It also ensures any inaccuracies made during these experiments can be known if future experiments don't achieve similar results as expected.

### 6.2.1 Single Particle

For the single particle Stokes speed experiment we start by dying the particles fluorescent so they can be seen easily under a black light. This is important in image processing as it allows the particle to be tracked much easier than under white light with a regularly dyed particle.

For this dying procedure, we used a fluorescent orange spray paint. A batch of particles in a specific size range are chosen to be painted, then a day is given to let them dry. Afterwards a specific particle is chosen, ideally as round as possible. We use image processing techniques laid out in Section 6.3 in order to determine the particle's radius. We are using glass particles with a density assumed to be  $2500 \text{ kg/m}^3$ , but further verification on this density should be done.

We use a silicone fluid with density which we verified to be  $971 \text{ kg/m}^3$ . The kinematic viscosity reported by the manufacturer is  $1000 \text{ cSt}$ . This is multiplied by its density to get a dynamic viscosity and units are converted to get  $0.971 \text{ kilograms per meter-seconds}$ .

This is enough information to calculate the Stokes speed of a given particle in this fluid. Note, if the Stokes speed seems too slow, we would use an alternative silicone fluid of  $100 \text{ cSt}$ , aiming to get experiments to last between 1 and 15 minutes.

After a particle is selected, and it's Stokes speed is calculated, we begin experimentally finding it's Stokes speed. Very special care is taken to keep the particle isolated, so as to not mix it up with a different one. The jar full of silicone oil is placed in a box which is spray painted black. There are two black lights on either side of the box directed at the jar. One side of the box is left open so the camera is able to film the experiment. When the setup is complete, all lights are turned off except the black lights to avoid any interference when it comes time for image processing. The camera should start filming, special care should be taken to ensure it is focused well on the jar and will be able to capture the particles entire journey to the bottom of the jar.

After these steps are completed, we set the particle on the top layer of the oil. This step has proven to be difficult at times. We use tweezers to grab the particle, but many particles have been lost as we attempt to place them in the jar. When the particle is set in the oil, in the center of the jar to avoid interactions with the glass walls, all that is left is to watch the particle slowly float to the bottom of the jar. After it reaches the bottom the experiment has concluded and the camera can be turned off. All that is left is image processing and to gather the results. This is continued in Section 6.3.



### 6.2.2 Bidisperse Hindered Settling

For the bidisperse hindered settling experiment, we undergo a similar process to the Stokes speed procedure with a few small changes.

To dye the particles, instead of using fluorescent spray paint, like before, we use glow in the dark (GITD) dye. The process is similar to Section 3.2 so the details are omitted here.

Once the two species of particles are dyed and sieved, we select the size range to use for our experiment. There was an abundant amount of particles in the range 200-250 micrometers and 300-355 micrometers, and this range is far enough apart to observe difference in settling, so we move forward with these sizes. We calculated the Stokes speed of the smaller particles to get an estimate of the length of the experiment.

Initially, the 1000 cSt oil was going to be used, however we found it would take too long for the experiment to run given the size of the particles so we switched to 100 cSt oil. The overall behavior of the two oils is very similar so we thought it reasonable to make the switch.

The larger particles were dyed GITD Green, while the smaller ones were GITD Blue. In white or black light, they appear almost identical. However, after being charged under the black light for a few minutes, all lights can be turned off and the particles are seen to shine very brightly as seen in Figure 19. While this is useful for capturing a quick photo of the particles positions, this affect only lasts a short period, and the particles must be re-charged in order to get the colors to shine brightly again. However, for our purposes of collecting qualitative results, this works fine.

After the particles are dyed, we pour the oil in a jar, making sure the jar is as clean as possible. The particles are then slowly mixed in, stirring as being poured into the oil to allow as many air bubbles to be removed as the mixing occurs. We should be left with a jar filled with our desired oil, and two different species of particles. We are working with a particle fraction of 0.17 and a 50/50 mix of both particles.

When the jar has been prepped, the particles should be well mixed and charged under a black light.

After approximately 15 minutes, the particles should be well mixed again, and the experiment is ready to commence.

Ensure the camera is capturing video and well focused on the jar, and ensure the camera settings are well suited to film in low-light. We use the following settings: aperture 4.5, ISO 12800, and 1/8 shutter speed. Ensure we are beginning with the particles well-mixed and turn off all lights so the GITD dye can take effect. The particles will eventually dim, it is recommended when the color of the two particles is no longer apparent to turn the black lights back on so as to recharge the particles. After only about a couple minutes these lights can be turned off once more so the GITD dye can be activated once more.

To acquire qualitative data, it should be recommended to find a longer lasting method for the GITD dye, as it only stays activated for a few minutes and the experiment can last up to 20 minutes.

The same jar of particles can be remixed and the experiment done again without replacing the oil or particles inside the jar. This should save quite a bit of time for future experiments as the preparation of the jar is by far the most time-consuming part of this experiment.

As mentioned in Section 6.1.3, for future experiments, it would be interesting to see specifically how the particle fraction effects the settling speed of particles, as well as the effects of using particle in Brownian vs. non-Brownian systems.

### 6.3 Image Analysis/Results

There are two parts to the image processing when attempting to get the Stokes speed of a particular particle, which is the first step in research to be done in Hindered-Settling. First, we must find the radius of the particle we are using in order to calculate the Stokes speed. When gravitational, drag, and buoyancy forces are balanced the particle achieves Stokes speed. This is found in Equation (50). For our case, we are using 1000 cSt oil and glass particles at a reported density of 971 and 2500 kilograms per cubic meter respectively. The only parameter left for us to find is the radius of our particles.

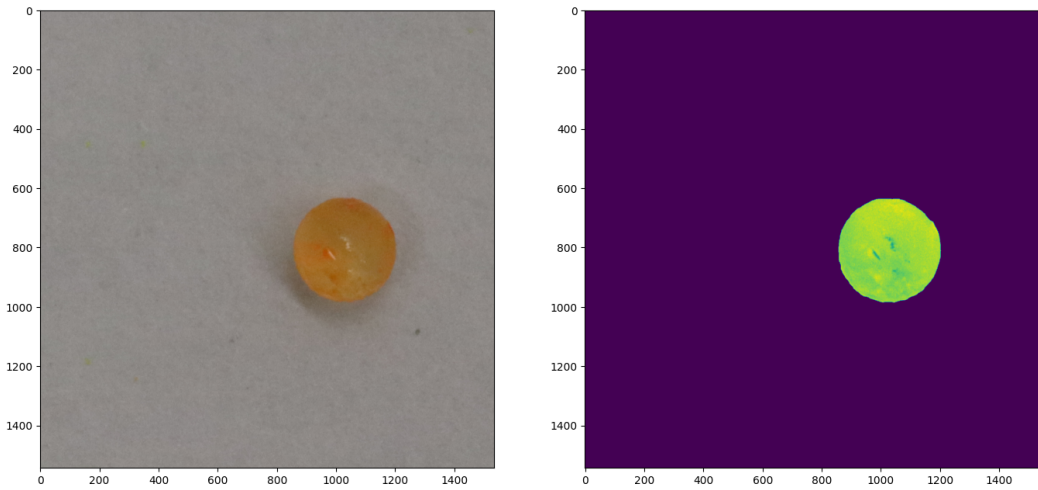


Figure 20: Zoomed in photo of particle and thresholded particle

We start this process by capturing a photo of the particle we wish to measure that has some scale in frame. We use graph paper with cm x cm squares and lay the particle in one of these squares. From here, there are many ways of finding the scaling factor, we opt to do connected component analysis to find the width and height of the square containing the particle. Using this, we take an average of the two so we find

the number of particles in a centimeter, and thus acquiring our scale. The next step is acquiring the radius of the particle.

From Figure 20 it is clear how we can find the pixels inside of the particle via thresholding. By selecting a certain threshold, perhaps using a certain color channel, we can remove the background from the image to isolate the particle. From here, we have two ways of finding the radius of the particle that agree fairly closely depending on the roundness of the particle. We can take an average of the distance from the highest and lowest and from the left and right most pixels of the particle then cut that in half. Alternatively, we can find the area by finding the number of pixels from the thresholding and use the well known formula  $Area = \pi r^2$  to find the radius from this. In both cases, we apply our scaling factor afterwards to find the radius of the particle in meters. Thus, we have all the necessary parameters to calculate the Stokes speed of a given particle.

Next, we wish to experimentally calculate the Stokes speed of our particles. The procedure is outlined in Section 6.2, we follow this procedure, making sure the particle is visible to perform the tracking.



Figure 21: Particle Falling at Stokes Speed

Since Stokes speed is when the particle reaches a constant velocity and the transient period it takes to get the particle to Stokes speed is so quick, we experimentally find the Stokes speed by plotting the particles position over time and performing a linear regression, the slope of this line should be our Stokes speed. To get these positions, we can perform a thresholding on each frame of the video, isolating the particle, and finding where the center of the particle is in our jar. To get the distance to pixels conversion, we have to include a ruler in the oil for at least a frame after the experiment.

We use as much of the ruler as possible to get the scaling, as when we use larger objects the error in selecting the top/bottom of the object has less of an effect. Typically, we would include the ruler at the end of the experiment so as not too make a mess with the oil while dropping the particles and potentially getting oil on the sides of the glass, messing with image processing. It is also important that the ruler is included in the center of the jar, so any warping due to the glass or change in scaling issues in distance simply due to positioning of the ruler can be ignored.

Special care is taken to keep close track of the fps the video is taken in, and if any trimming is done, the overall time step of each frame. Thus, we have a time scale in seconds while the particle travels and a distance scale in millimeters as the particle travels downwards. Using all of this, we are able to go from meaningless measurements, like pixels per frames, and convert them to measurements we can compare with our calculated Stokes speed such as millimeters per second. After this we can continue on and graph the particles position. After which we perform the linear regression as seen in Figure 22 and are able to obtain the experimentally found Stokes speed.

The calculated and experimental stokes speed of particles from two different size ranges are compared in Table 5. It is clear that the calculated Stokes speed is consistently larger than the experimental Stokes speed. There are many reasons this could happen, which we speculate at the end of this section.

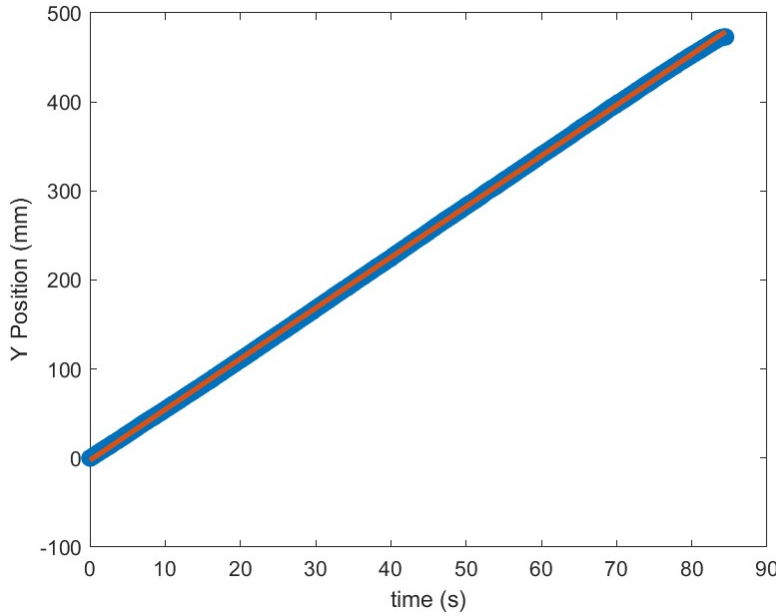


Figure 22: Particles position through time along with linear regression

From Table 5 we found that the Calculated Stokes speed of the particles were consistently much larger than what we experimentally found it to be. We attribute this error to a misreported viscosity from the manufacturer of the silicone oil. To gather a more accurate viscosity, we adjust the viscosity term in order to minimize the mean squared error of the calculated and experimental Stokes speed. For GSB-1 particles we found  $\eta_{GSB1} = 1.178$ , for the GSB-3 particles  $\eta_{GSB3} = 1.297$  and by minimizing the mean squared error of all particles, we get  $\eta \approx 1.183$ .

We also report the Reynolds and Péclet numbers for each particle in Table 5, where we use equations (54) and (55). We use the average radius of a particle for  $r$  and our experimentally found viscosity of  $\eta = 1.183$ . We also use the experimentally found Stokes speed of the particle in calculations. We note that the Péclet number of all our particles are well above  $Pe_c$ , so we are dealing with particles in the non-Brownian systems.

Particle-Type	Radius (mm)	Calculated Stokes Speed (mm/s)	Experimental Stokes Speed (mm/s)	Error Fraction	Re	Pe
GSB-1	0.891 - 0.990	2.731 - 3.372	2.5210	1.083 - 1.338	0.00194	$1.217 \times 10^{13}$
	0.887 - 0.985	2.7034 - 3.3375	2.4394	1.108 - 1.368	0.00188	$1.166 \times 10^{13}$
	0.909 - 1.010	2.8399 - 3.5060	2.5449	1.116 - 1.378	0.00189	$1.279 \times 10^{13}$
	0.874 - 0.971	2.6265 - 3.2426	2.5261	1.039 - 1.284	0.00191	$1.173 \times 10^{13}$
	0.883 - 0.981	2.6746 - 3.302	2.4297	1.101 - 1.359	0.00186	$1.152 \times 10^{13}$
GSB-3	0.4086 - 0.4540	0.5742 - 0.7088	0.4611	1.245 - 1.537	0.000164	$4.680 \times 10^{11}$
	0.4422 - 0.4913	0.6789 - 0.8382	0.5202	1.305 - 1.611	0.000359	$6.184 \times 10^{11}$
	0.4125 - 0.4583	0.5851 - 0.7224	0.5022	1.165 - 1.438	0.000199	$5.195 \times 10^{11}$
	0.4095 - 0.4550	0.5766 - 0.7119	0.4959	1.163 - 1.436	0.000176	$5.055 \times 10^{11}$
	0.4629 - 0.5143	0.7368 - 0.9096	0.6395	1.152 - 1.422	0.000257	$8.330 \times 10^{11}$

Table 5: Results of various particle size Stokes speed

In both parts of image analysis, we have attempted to eliminate as much error as possible, however each

step will contain some amount of error. In getting the particle radius, we have to find a scaling for pixels to meters. This is likely the largest contributor to error, as there is only so much precision in the printing of these boxes. We initially assume the box has width and height of 1 cm, as this is how they were designed. However, in the printing, the ink could have bled across, shrinking the interior of the box by as much as 1 mm. We use these possibilities of box width to get the range of radius, and thus calculated Stokes speed that we use in Table 5.

For getting the radius of the particle, we rely on thresholding to remove error in the measurement of radii and visually certify the thresholding correctly removed the background, including the shadow cast by the particle. This is seen in Figure 20 as the background is clearly removed from the image of the particle.

From the image processing of the experimental section, most error is again likely to come from finding the scaling factor. We attempt to use as much of the ruler in the oil to acquire our scale as possible to remove this error, but a small amount of error could still occur in the selection of the ruler length.

Further error occurring between discrepancies in experimental versus calculated results are likely to come from the roundness of the particles. Since the calculated Stokes speed assumes the particle is perfectly round, any non-roundness of the actual particle will cause some error.

The final area of expected error is any misreported parameters. We certified the density of the fluid and particles was accurate (however, the density of a single particle might vary by some small amount). We noted possible error in viscosity and worked on recalculating that to fit well with the data. The radius could also be off by a small margin due to errors in measurement, but these errors were accounted for. In future research on this topic, it is important to note these possible sources of error and they should be accounted for.

## 7 New & Future Research

### 7.1 Improvements of Experimental Procedures

Collecting robust and accurate data is key to any future work upon this project. The proper acquisition of data is especially important for the mass shedding project, where little existing theory is available to inform models. After performing numerous experiments over the past weeks, the group has come up with numerous suggestions for how the experimental apparatus can be further developed and refined.

One issue the group faced frequently when performing mass shedding experiments was the termination of an experiment, due to a part of the fluid front reaching the end of the track, while the remaining slurry clearly shows more potential to shed. This is especially problematic for experiments at especially high volume fractions, where experiment generally last much longer - and complete their shedding over longer time scales than low volume fraction shedding experiments. Premature termination of experiments can lead to inaccurate measurements of the total mass shed during experiment, creating bad data. This bad data could explain why, for experiments with the BSLZ-3 ceramic particles at an angle of 55 degrees, an unexpected decrease in total mass shed was seen past a volume fraction of 0.40. It is possible these higher volume fraction experiments still have the potential to shed more - and simply cannot due to the low track length. To improve this, an extended track could be created, in order to allow experiments to last over long time periods. Facilitating experiments over longer time periods could also provide insight into other experiments - like the bidisperse experiment - and give insight into the long term behavior of separate particle fronts.

An aspect of the mass shedding experiment specifically that could be majorly improved is the mass measurement system. Currently, the group is using a very rough set up, using a large plastic lid placed upon a scale. With the current set up, the output of the scale is recording using a GoPro camera, and visually inspected to find the measurements. This is a costly way to store information about tests data wise, and is a huge time sink. Multiple improvements could be made to this set up that would not only improve the quality of the data acquired but improve the testing process as a whole. A simple but potentially expensive improvement would be to replace the current scale with one that has a higher resolution, and can output data to a computer as a time series. The current scale only has a precision of one decimal point - which does not provide an accurate weight measurement, and can even neglect particularly small sheds. Outputting data as a time series would forgo the need for the GoPro, saving data in a much more efficient format that can be immediately analyzed by groups. A likely cheaper improvement would come from replacing the catch for the mass. A new catch that is larger than the current one, and can better absorb the impact of the shed clumps, would benefit the set up. A larger catch would help eliminate the risk of a mass potentially missing the scale - which has happened in prior trials - and keep the group from losing data. A catch with the ability to better absorb the impact of the masses, would be helpful with a more precise scale - which would likely be more sensitive to impact than the old scale.

Another problem faced in the mass shedding experiments was finding the laser height profile to observe if there was a correlation between the height of the ridged particle front and when a mass would shed. We attempted to capture a large length of the track, and while the video was seemingly fine, the end result was a distorted mass profile as the camera distortion towards the edges of the ramp might have played a role in giving us trouble with image processing. To solve this, in the future, we will capture a more narrow range of values, such as between 10cm and 30cm. On top of that, using a penny to calibrate the images and convert the pixels of frame to a length created problems due to the small size. Towards the end of the program, we switched to using 3 quarters stacked vertically on top of each other, but to make it more simple, an easy 3D printed block can be used to calibrate the entire track easily. As a general rule with calibration, there will always be more error the thinner the object is when you have to manually calibrate and select where an object begins/ends. This is very similar to the hindered settling experiment, where initially, we tried to use the particle diameter to calibrate the pixels per inch scaling. The problem is that the particle was so small that a difference of one or two pixels can create drastic differences in the ppi conversion, which the group suspect happened as well with using the height of a single penny to calibrate the laser height.

## 7.2 Future Mass Shedding Experiments

After improving the experimental procedure, the group has extensive plans for testing going forward. First, the group hopes to test a wider range of particles sizes for each of the existing materials tested. Numerous other sizes of glass particles exist, such as the larger GSB-3 and smaller MIL-7 particles, and experimenting with varying size could give greater insight into the affects of particles size on mass shedding. Currently the group does not plan to try ceramic particles of other sizes, unless they are able to order larger particles, as the smaller ceramic particles available to us do not shed when tested. Another potential direction would be to test particles composed of new materials with densities different to the glass and ceramic particles. This direction would provide more robust data, upon which the group could gain insight into how density affects the behavior of the slurry and masses. Going forward, the group also hopes the measure the velocity of the front and of the sheds, in order to use that as another measurement upon which we will be able to perform analysis. To do this accurately, recording the film at a higher frame rate and writing code to accurately track

the shedded mass's distance over time will be the next steps going forward. This will also require running multiple trials of the same experiments to accurately observed the area in which mass is shed, so that the camera can have a close up shot of it shedding and falling down the remaining length of the track. It could be helpful to increase this length to allow for less error in velocity calculations. We can then compare this data to that observed by a mass sliding down a lubricated incline to see if the experimentally derived velocity correlates to a solid particle.

### 7.3 Mass Shedding Models

When it comes to creating mass shedding models we have two different goals. The first goal we hope to achieve is to develop a model describing the dynamics after the phase transition into the “max-packed ridged regime”, focusing explicitly on the mass shedding. The second, and admittedly harder, goal we hope to achieve is to develop a model describing the entire dynamics of the particle laden flow that can describe both phases.

Focusing on the first goal, we considered that the mass shedding seen in our particle laden flow experiments may be similar to chunks of ice breaking off the edge from a glacier, as seen in the papers [2, 3, 15]. In particular, we focused on the paper [3], which has a unifying framework for iceberg calving. In particular, it describes a velocity balance between the vertically averaged terminus velocity, calving rate and melt rate of the vertical face of the terminus as seen in Figure 23. The change in calving position in time is given by the following differential equation

$$\frac{d\mathbf{X}}{dt} = \mathbf{u}_t - \mathbf{u}_c - \dot{\mathbf{m}}, \quad (57)$$

where  $\mathbf{X}$  is the terminus position,  $t$  is time, and  $\mathbf{u}_t$ ,  $\mathbf{u}_c$ ,  $\dot{\mathbf{m}}$  are the vertically averaged terminus velocity, calving rate and melt rate of the vertical face of the terminus. Bold face is used to indicate two-dimensional horizontal vectors; whenever the horizontal axes are oriented along a flowline, these vector quantities are expressed as (non-bold) scalars. We note that over annual timescales, terminus velocity and calving rate tend to scale with each other, so we tend to see equilibrium or near equilibrium cases in the real world. An idea from this model that seems especially applicable to the mass shedding problem is the idea of the existence of two critical values for the width of the terminus. The first width -  $H_0$  - is a width that determines where calving initiates, while the second width -  $H_1$  - determines where calving ends. Both widths define the extend of the glacier created by a calving event. This idea matches what is seen in mass shedding experiments, where shedding appears to begin when part of the front reaches a certain width. Further more, this matches how each shedding event ends when the part of the mass attached to the front decreases to a particular width and pinches off. An idea similar to this concept from the paper could serve to guide and inform a possible shedding model. Figure 23 shows this idea.

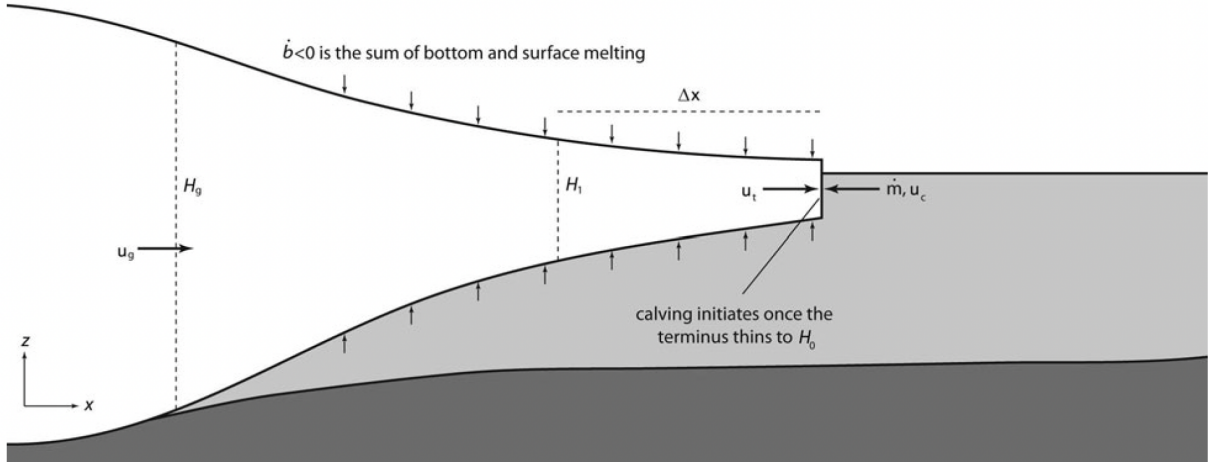


Figure 23: Schematic diagram of a glacier terminus indicating many of the variables used in the present analysis from [3].

However, this is quite a general framework for describing shedding, and the ice melting describes a flow we don't necessarily see with our particles. Therefore this model may not be the best model to use since we are working with what could also be described as well-packed granular media (although there is still an underlying fluid, its effects may become negligible). As a result, we may not get any fluid effects describing the mass shedding and instead find granular media effects such as stresses occurring along chains of particles. Whether one model describes monodisperse mass shedding effects better than another is to be determined.

## 8 Conclusion

In this project, we conducted numerous experiments in order to better understand the bidisperse model, the mass-shedding phenomenon and experimentally determining Stokes speed and hindered settling functions.

Over the course of around 30+ mass-shedding experiments, we developed a better understanding of when mass sheds occur, how much mass is shed as well as when and where it sheds. Over around 20 bidisperse experiments, we developed a better understanding of how the particles settle to equilibrium, how they display the Brazil nut effect, when we get clear separation between particle fronts, as well as obtained data that could be used to develop models concerning the evolution of the system. We ran around 15 Stokes speed experiments to determine whether we could accurately predict particle Stokes speed to help us eventually accurately determine hindered settling speeds for many particles in a jar.

In addition, further work could be done in developing the model and equations that govern bidisperse particle laden flow. The empirical results and numerical methods explored in this project will be useful in motivating and validating the creation of this model. The data collected in our hindered settling project to verify stokes speed brings us closer to obtaining accurate data to continue analysing the bidisperse case and deriving a hindrance settling function for those experiments. This hindrance settling function has only been developed historically in the monodisperse case, but further research in the bidisperse case could prove very useful in the exploration of bidisperse particle laden flow.

We also would have liked to explore the bidisperse case on a spiral separator, a device used to separate particles of different sizes that is directly applicable to the mining industry in filtering specific ores. Our aim

was to design a spiral separator which we can conduct bidisperse experiments on. We also aimed to develop a theory for mass shedding to help describe the phenomenon after the ridge has formed and mass shedding begins (after the phase transition).

## Acknowledgement

We would like to thank our mentors Professor Andrea L. Bertozzi, Dr. Sarah Burnett, Dr. Lingyun Ding, and Evan Davis for their invaluable guidance and advice. We would also like to thank Jack Luong for developing the theory behind the bidisperse diffusive flux model in Section 2.3.

## References

- [1] A Acrivos, GK Batchelor, EJ Hinch, DL Koch, and Roberto Mauri, *Longitudinal shear-induced diffusion of spheres in a dilute suspension*, Journal of fluid mechanics **240** (1992), 651–657.
- [2] R.B. Alley, K.M. Cuffey, J.N. Bassis, K.E. Alley, S. Wang, B.R. Parizek, S. Anandakrishnan, K. Christianson, and R.M. DeConto, *Iceberg calving: Regimes and transitions*, Annual Review of Earth and Planetary Sciences **51** (2023), no. Volume 51, 2023, 189–215.
- [3] Jason M. Amundson and Martin Truffer, *A unifying framework for iceberg-calving models*, Journal of Glaciology **56** (2010), no. 199, 822–830.
- [4] T. A. Brzinski and D. J. Durian, *Observation of two branches in the hindered settling function at low Reynolds number*, Phys. Rev. Fluids **3** (2018Dec), 124303.
- [5] Albert Einstein, *Eine neue bestimmung der moleküldimensionen* (1905).
- [6] AB Holland-Batt and PN Holtham, *Particle and fluid motion on spiral separators*, Minerals engineering. **4** (January 1991), no. 3-4.
- [7] Herbert Huppert, *Flow and Instability of a Viscous Current Down a Slope*, Nature **300** (1982), 427–429.
- [8] Oded Katz and Einat Aharonov, *Landslides in vibrating sand box: What controls types of slope failure and frequency magnitude relations?*, Earth and Planetary Science Letters **247** (2006), no. 3, 280–294.
- [9] Laura Patricia Martínez-Padilla, *Rheology of liquid foods under shear flow conditions: Recently used models*, Journal of Texture Studies **55** (2024), no. 1, e12802, available at <https://onlinelibrary.wiley.com/doi/pdf/10.1111/jtxs.12802>.
- [10] Dima Merhi, Elisabeth Lemaire, Georges Bossis, and Fadl Moukalled, *Particle migration in a concentrated suspension flowing between rotating parallel plates: Investigation of diffusion flux coefficients*, Journal of Rheology **49** (2005), no. 6, 1429–1448.
- [11] N. Murisic, J. Ho, V. Hu, P. Latterman, T. Koch, K. Lin, M. Mata, and A.L. Bertozzi, *Particle-laden viscous thin-film flows on an incline: Experiments compared with a theory based on shear-induced migration and particle settling*, Physica D: Nonlinear Phenomena **240** (2011), no. 20, 1661–1673. Special Issue: Fluid Dynamics: From Theory to Experiment.
- [12] Nebojsa Murisic, Benoit Pausader, Dirk Peschka, and Andrea L Bertozzi, *Dynamics of particle settling and resuspension in viscous liquid films*, Journal of Fluid Mechanics **717** (2013), 203–231.
- [13] Ronald J Phillips, Robert C Armstrong, Robert A Brown, Alan L Graham, and James R Abbott, *A constitutive equation for concentrated suspensions that accounts for shear-induced particle migration*, Physics of Fluids A: Fluid Dynamics **4** (1992), no. 1, 30–40.
- [14] Constantine Pozrikidis, *Fluid dynamics: Theory, computation, and numerical simulation*, Vol. 2, Springer New York, NY, 2009.
- [15] Christian Schoof and Ian Hewitt, *Ice-sheet dynamics*, Annual Review of Fluid Mechanics **45** (2013), no. Volume 45, 2013, 217–239.
- [16] Jeffrey T. Wong and Andrea L. Bertozzi, *A conservation law model for bidensity suspensions on an incline*, Physica D: Nonlinear Phenomena **330** (2016), 47–57.